Fall 10-1-2020

Interpretations of Lava Flow Properties from Radar Remote Sensing Data

Gavin Douglas Tolometti
Western University, gtolomet@uwo.ca

Catherine Neish

Gordon R. Osinski
Western University

Scott S. Hughes
Idaho State University

Shannon E. Kobs-Nawotniak
Idaho State University

Citation of this paper:
Tolometti, G. D., Neish, C. D., Osinski, G. R., Hughes, S. S., & Nawotniak, S. K. (2020). Interpretations of lava flow properties from radar remote sensing data. *Planetary and Space Science*, *190*, 104991.

Interpretations of Lava Flow Properties from Radar Remote Sensing Data

G. D. Tolometti[a,b*], C. D. Neish[a,b], G. R. Osinski[a,b], S. S. Hughes[c], S.E. Kobs Nawotniak[c]

[a]Department of Earth Science, University of Western Ontario, London, ON, Canada

[b]Institute for Earth and Space Exploration, University of Western Ontario, London, ON, Canada

[c]Dept. of Geosciences, Idaho State University, Pocatello, ID, USA

*Corresponding author

Email address: gtolomet@uwo.ca (Gavin D Tolometti)

Postal address: Biological & Geological Sciences Building, Room 1026. 1151 Richmond Street N. London, Ontario, Canada, N6A 5B7

Abstract

The surface morphology and roughness of a lava flow provides insight on its lava properties and emplacement processes. This is essential information for understanding the eruption history of lava fields, and magmatic processes beneath the surface of Earth and other planetary bodies such as the Moon. The surface morphology is influenced by lava properties such as viscosity, temperature, composition, and rate of shear. In this work, we seek to understand how we can interpret the emplacement processes and lava properties of lava flows using remote sensing data. Craters of the Moon (COTM) National Monument and Preserve in Idaho hosts a suite of compositionally diverse lava flows with a wide range of surface roughness making it the ideal case study. Lava flows there have surface morphologies consistent with smooth pāhoehoe, slabby pāhoehoe, hummocky pāhoehoe, rubbly pāhoehoe, \`a\`ā, block-\`a\`ā, and blocky textures. The variation in surface roughness across the lava field reflects changes in lava properties and/or emplacement processes over space and time. We investigate geochemical and petrographic variations of the different lava flow morphologies and analyze how they relate to airborne radar data. Results show L-Band (24 cm) radar circular polarization ratios (CPR) distinguish the contrasting surface roughness at COTM, separating the smoother (primitive; low SiO_2 and alkali) and rougher (evolved; high SiO_2 and alkali) lava flows. However, ambiguities are present when comparing the CPR values for rubbly pāhoehoe and block-\`a\`ā flow. Even though their CPR values appear similar at the decimetre scale, they have distinct morphologies that formed under different emplacement processes. Without ground-truth information, the rubbly pāhoehoe and block-\`a\`ā lava flows could therefore be misinterpreted to be the same type of flow morphology, which would lead to false interpretations about their lava properties and emplacement processes. This is important when comparing these flows to lava flows on other planetary bodies that share similar CPR values, such as the Moon. Thus, using terrestrial analogues such as those at COTM can provide an improved understanding of the surface morphology and emplacement processes of lunar lava flows. This will lead to more refined interpretations about past volcanic processes on the Moon.

Keywords: Lava flow, Craters of the Moon, Morphology, Surface roughness, Radar

1 Introduction

The lava properties and emplacement processes of volcanic features on Earth and other planetary bodies are often inferred from their surface roughness (Griffiths and Fink, 1992; Crisp and Baloga, 1994; Keszthelyi et al., 2004; Guilbaud et al., 2005; Khan et al., 2007; Campbell et al., 2009; Harmon et al., 2012; Lawrence et al., 2013; Neish et al., 2017). The scale of surface roughness can vary on a single lava flow and reflect multiple factors that may have influenced it during an eruption (MacDonald, 1953; Gregg and Fink, 1995, 1996; Sehlke et al., 2014). Thus, understanding the formation of surface roughness features at different scales can help justify interpretations about lava properties (e.g., composition, density, viscosity) and emplacement processes (e.g., mechanical fracturing, viscous tearing).

Lava flow surface roughness is defined at a range of scales. Centimetre scale roughness (e.g. crescent ripples and folds) is produced when the lava encounters small topographic obstacles and when a (plastic) crust of a few mm thickness is deformed during cooling (Fink and Fletcher, 1978; Gregg et al., 1998). Smooth pāhoehoe surfaces typically form from lavas with low silica content and low viscosity, erupted at temperatures near the liquidus of basalt (1200°C) (Tilley and Thompson, 1970). Changes in roughness at the decimetre scale (e.g. clinker \`a\`ā fragments) require extensive disruption of the lava flow crust. In contrast to smooth pāhoehoe, rough \`a\`ā forms when lava is ruptured due to increasing viscosity or rate of shear as the lava cools and degasses (Peterson and Tilling, 1980; Rowland and Walker, 1990; Sehlke et al., 2014). Highly siliceous blocky lava flows (>55 wt% SiO_2) disrupt their surfaces due to creep fracturing, which typically form decimetre to metre-sized polyhedral blocks with smooth faces (MacDonald, 1953). However, viscous rupturing and creep fracturing are not the only mechanisms to produce rough flows. Rough lava can also form through the mechanical fracturing of a solidified pāhoehoe crust, producing a class of lava flows known as transitional lava flows (Keszthelyi *et al.*, 2004; Guilbaud *et al.*, 2005). These flows often exhibit “rubbly” or “slabby” textures, with pāhoehoe crust fragments ranging from tens of centimetres to metres in size (Keszthelyi et al., 2004; Guilbaud et al., 2005; Hamilton et al., 2013; Robert et al., 2014; Neish et al., 2017). Transitional pāhoehoe lava flows studied in Iceland (Keszthelyi et al., 2000, 2004; Guilbaud et al., 2005), Idaho (Neish et al., 2017), Hawaii (Peterson and Tilling, 1980), and India (Duraiswami et al., 2014) exhibit surfaces with metre-sized slabs of pāhoehoe crust, fractured by lava flow inflation (Keszthelyi et al., 2004). Rubbly pāhoehoe textures can form in sequence after slabby pāhoehoe if the crust is extensively fragmented. In some cases where lava flows have been degraded and/or buried, rubbly pāhoehoe has been falsely interpreted as \`a\`ā (Bondre et al., 2004; Duraiswami et al., 2008). Their similarities in brecciated surfaces and roughness scale can make them almost indistinguishable when eroded. Table 1 summarizes the surface roughness and morphologies of lava flows documented in the field on Earth.

When field observations are not available, radar data can provide important information about lava surface roughness at different scales. This is especially relevant for other planetary bodies where ground truth is limited or non-existent. Radar data has been used to distinguish and quantify the surface roughness of lava flows on planetary surfaces to interpret their lava properties and emplacement processes. For example, Earth-based radar data has been used to map and analyse the distribution of lava flows on the lunar surface. Morgan et al. (2016) and other workers (Campbell et al., 2009, 2007) used Arecibo P-band (70-cm) radar to penetrate through the lunar regolith and map the lava flow boundaries in lunar mare using same-sense circularly polarized (SC) radar data. In Figure 1, circular polarization ratios (CPR) calculated from returned Arecibo P-band radar data show the variations in metre-scale lava flow surface roughness in the Mare Imbrium. Lava flows with moderate-high CPR (~0.5) indicate rough surfaces while lava flows with low CPR (< 0.5) indicate smooth surfaces. These values can be compared to radar data of terrestrial lava flows, to aid in the interpretation of the properties of lunar lava flows. Thus, understanding the roughness characteristics of different surface morphologies at a range of scales can help distinguish why some flow morphologies have similar CPR values, which can improve our inferences on the volcanic surface features on planetary surfaces, and refine the interpretations made using remote sensing methods.

Depending on the remote sensing method used, the surface roughness values can vary, which will ultimately influence interpretations about lava properties and emplacement processes. On Earth, we can quantify surface roughness using a suite of in-situ, airborne, and satellite remote sensing instruments. For example, remote sensing methods such as LiDAR have been used to distinguish and quantify surface roughness of lava flows at different resolutions and scales (Glenn et al., 2006; Glaze and Baloga, 2007; Rosenburg et al., 2011; Whelley et al., 2014, 2017). However, for studying other planetary surfaces, radar is the only remote sensing technique capable of quantifying roughness at the decimetre scale. Decimetre scale surface features are too small to observe with presently available visible imagery; the highest resolution cameras provide data at 0.5-1 m resolution (Chin et al., 2007; McEwen et al., 2007). Thus, radar datasets are critical to infer the decimetre scale surface roughness of lava flows on other planetary bodies (Campbell et al., 2009, 2010; Carter et al., 2012; Harmon et al., 2012; Neish et al., 2014, 2017).

Lava Flow Morphology	Description	Surface Roughness Scale
Smooth Pāhoehoe	A smooth lava flow with a thin, glassy crust that may collapse due to inflation or strength instability; cm-scale ropey textures form on the surface while the flow is in motion.	Lava flow appears smooth at km- and m-scales. Small features such as ropey and spiney textures make the lava appear rougher at cm- and mm-scales.
Hummocky Pāhoehoe	Undulating pāhoehoe lava comprising lava toes, small lobes, and tumuli. The surface morphology resembles a bulbous shape where lava has risen by a few m to tens of m and connected by steep troughs. Lava is also referred as a 'bulbous' pāhoehoe flow.[a]	Lava flow appears smooth at km-scales. Hummocks make the lava flow relatively rough at m-scales while the pāhoehoe textures described above make it rough at cm-scales.
Rubbly Pāhoehoe	A lava flow with a preserved flow base and brecciated pāhoehoe crust.[b] The surface becomes fractured and brecciated due to disruption from syn- or post-emplacement processes. Common in flow fields with linear volcanic vent systems.[c]	Lava flow appears roughest at m and dm-scales.
Slabby Pāhoehoe	Metre to kilometre-sized slabs of pāhoehoe crust, which were fractured, tilted, and carried by an advancing or draining underlying lava.	Rough at m- and km-scales and smooth at cm-scales (notwithstanding ropey and spiney textures described above).
\`A\`ā	Lava flow with a rough clinkered surface formed by the development of a yield strength and increase in viscosity.[d] Interior becomes viscously torn as it advances further from its source.	Lava flow appears roughest at m and dm-scale. Similar dm-scale roughness to rubbly pāhoehoe.
Blocky to High Relief \`a\`ā (Block-\`a\`ā)	Rough and jagged with occasional vesicular (>70%) froth, and weakly conchoidal fractures.	Conchoidal fractures and rough jagged surface appear rough at m- to dm-scale.
Blocky	Lava flows covered with a broken carapace of decimetre to metre-sized fragments with smooth faces and dihedral angles.	Lava is rough at dm- and m-scales. Block surfaces smooth at cm-scales.

Table 1. Descriptions and surface roughness scale of lava flow morphologies on Earth are summarized from measurements of crustal material on their surfaces and notes taken in the field. [a]Kuntz *et al.* (2007), [b]Guilbaud *et al.* (2005) and Duraiswami *et al.* (2008), [c]Keszthelyi *et al.* (2000), [d]Sehlke *et al.* (2014). For more field descriptions and detailed discussions on the lava flows surface morphologies refer to Kilburn (2000) and Harris *et al.* (2017).

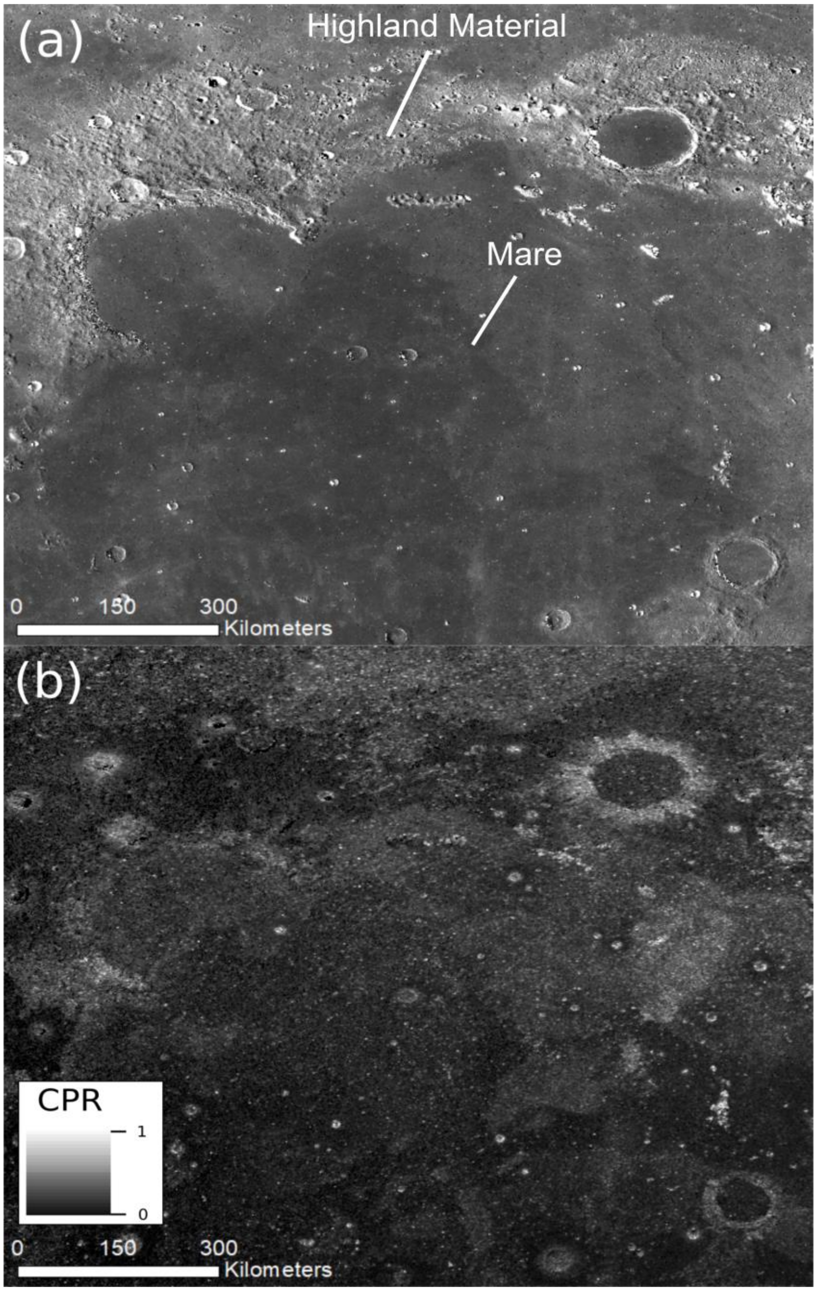

Figure 1. Mare Imbrium lava flows revealed using Earth-based radar: (a) Lunar Reconnaissance Orbiter Wide-Angle Camera mosaic (100m/pixel) of the Mare Imbrium. (b) Arecibo P-Band radar data (70 cm wavelength, 200 m/pixel) of the same region. The lava flows in the mare have large variation in their CPR values, which suggests a range of surface textures. Flows with high CPR are rough, while those with low CPR are smooth at the decimetre-scale. Highland and mare material are labelled reference; the low CPR in the highlands is not indicative of the presence of smooth lava flows.

Generalized relationships between surface roughness, composition, petrographic textures, and crystallinity in lava fields have been discussed for flows located in areas such as Iceland (Keszthelyi et al., 2000, 2004; Guilbaud et al., 2005), Hawaii (Peterson and Tilling, 1980; Cashman et al., 1999; Robert et al., 2014; Sehlke et al., 2014), and Guatemala (Soldati et al., 2016). These studies suggest that increasing microcrystallinity and decreasing temperature with distance from the vent cause increases in viscosity and yield strength, which result in increased surface roughness at the centimetre-metre scale. On the other hand, transitional lava flow surface roughness formed by syn- or post emplacement processes such as changes in effusion rates, pāhoehoe crust inflation, and topographic variability, can produce similar surface roughness for very different reasons. This may lead to misinterpretations about the style of volcanism in regions where there is little or non-existent ground truth and where we must rely on remote sensing data such as radar.

Our chosen field site, Craters of the Moon (COTM) National Monument and Preserve in Idaho, is a 1650 km^2 polygenetic lava field with cinder and spatter cones, non-eruptive fissures, lava tubes, and basaltic lava flows of varying compositions emplaced from 15–2 ka (Leeman et al., 1976; Greeley and King, 1977; Kuntz et al., 1982, 1992; Kuntz, 1989; Hughes et al., 2002) (Figure 2). The lava flows display blocky, block-`a`ā, `a`ā, and rubbly, slabby, hummocky and smooth pāhoehoe morphologies (Kuntz, 1989; Kuntz et al., 2007). The compositions of the individual lava flows vary with respect to SiO_2, MgO, FeO, TiO_2, P_2O_5, and Th (e.g. SiO_2 ranges from 45 wt% to 65 wt%) (Reid, 1995; Hughes et al., 1999; Putirka et al., 2009) with blocky and block-`a`ā lava flows exhibiting SiO_2 content >55 wt% (Stout et al., 1994). Research conducted by previous workers has proposed that fractional crystallization (Leeman et al., 1976; Hughes et al., 2002), country rock assimilation (Leeman, 1982; Kuntz et al., 1986), and/or evolved magma reservoirs (Kuntz et al., 1982; Kuntz et al., 1986) are responsible for the different compositions. Hughes et al. (2016) described some of the northernmost lava flows as chemically evolved latites (aka trachydacite) based on MgO and TiO_2 contents and suggested that their compositions reflect hybridized crystallization due to crustal contamination, magma mixing, and long-term fractionation in crustal magma reservoirs. Extensive work on the geochemistry of the lava flows at COTM has provided a general understanding of their magmatic origin and processes, but to date, little work has focused on the diversity of their surface morphologies and roughness.

In this work, we investigate the surface roughness of lava flows in the northernmost part of COTM, to further our understanding of how surface roughness properties correlate to the petrography and geochemistry of a lava flow, and whether these are distinguishable using radar remote sensing data. We then use this information to discuss what interpretations can be made if we are restricted to using radar data to infer the lava properties and emplacement styles of lava flows on other planetary bodies.

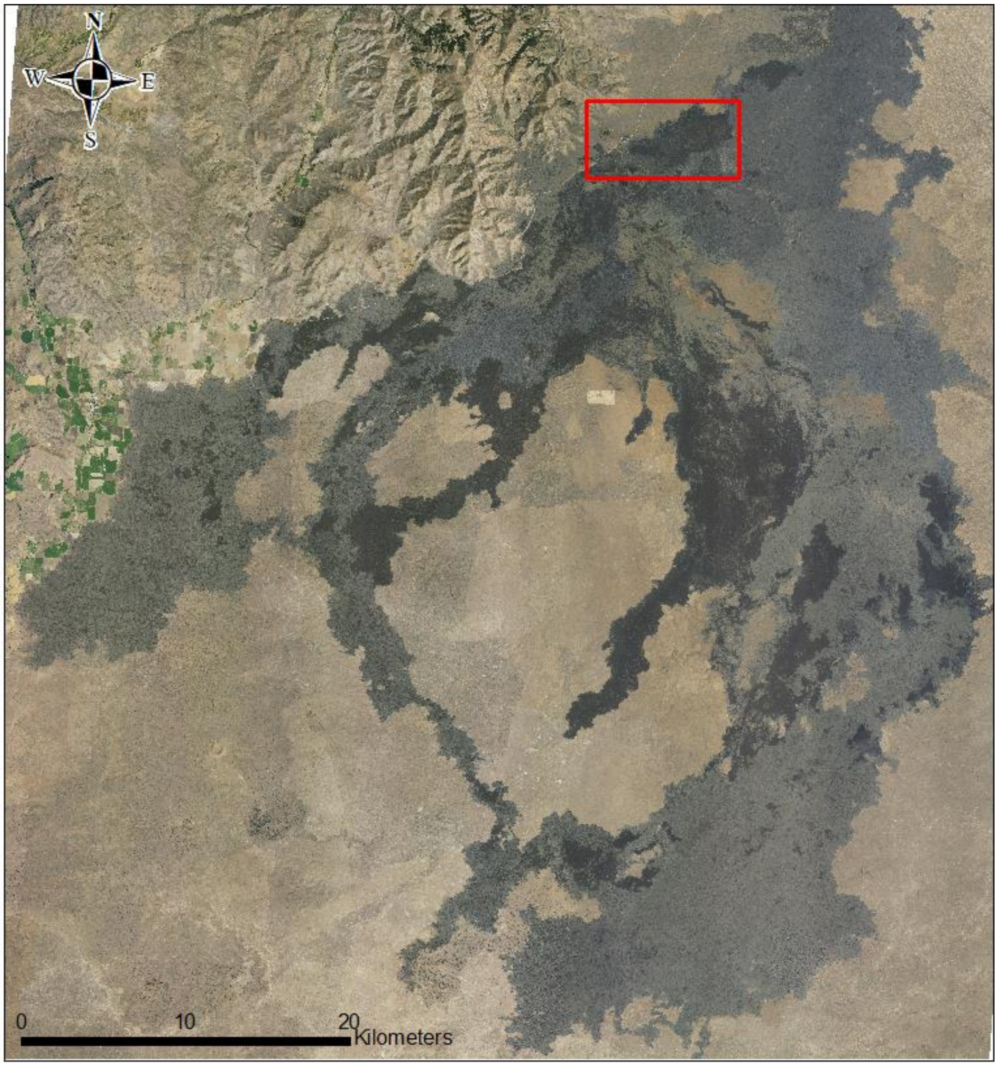

Figure 2. Overview of our field study area at Craters of the Moon National Monument and Preserve, Idaho. National Agriculture Imagery Program (NAIP) data of COTM acquired in 2015. The red box outlines the field area for this study. Field site coordinates: 43.2058° N, 113.5002° W (see Figure 3).

2 Methods

2.1 Field sampling

Field work was conducted in August 2016 and 2017 at COTM. A total of fifty-three hand samples were collected from five lava flows: Big Craters (Rubbly pāhoehoe), Blue Dragon (Smooth pāhoehoe), Highway (Block-`a`ā), North Crater (Hummocky pāhoehoe), and Serrate flow (Blocky) (Figure 3). Due to accessibility (many of the lava flows were difficult to traverse on foot), the majority of the sampling was conducted 10 m to ~100 m from the lava flow margins; a small number of samples were collected closer to the flow center where the terrain allowed for easier access. As many samples as possible were collected in each studied lava flow. This was done to look for any variations in the petrographic and geochemical data. For the petrography and geochemistry of the samples to best represent the interior of the lava flow, sampling was restricted to >5 cm below the lava crust. This is important because the geochemistry and petrography of the quenched lava flow crust only represents the rapid cooling of the lava on the surface and not the interior that remained molten for a longer period. In addition, the surface roughness is less influenced by the petrography and geochemistry of the quenched crust, but rather the mechanical processes disrupting it during flow emplacement. Comparing the geochemistry and petrography of the crust to the remote sensing data would not provide insight into how the lava properties of the lava flow influenced its surface morphology and roughness.

2.2 Petrographic and geochemical analyses

From the fifty-three hand samples, twenty-three polished thin sections were prepared for petrographic analysis. Mineral mode (%), crystallinity (%), volcanic glass (%), vesicularity (%), and mineral size (mm-cm) were estimated for each sample by point counting on a 1000-point grid in each of the polished thin sections. Backscattered electron (BSE) images were used to study the microlites in the volcanic glass, as well as to record petrographic textures that were not observable with optical microscopy. Microlite compositions were determined by electron probe micro-analysis (EPMA) (15 kV, 20 nA, 5 µm spot size, standards: Albite – Si, Al, and Na; Rutile – Ti; Fayalite – Fe; SanCarlos – Mg; Rhodonite – Mn; Anorthite – Ca; Orthoclase – K, Celesite – Sr; Barite – Ba) using the JEOL JXA-8530F field-emission electron microprobe at the University of Western Ontario.

Thirty-eight of the fifty-three samples were prepared for X-ray fluorescence (XRF) analysis to obtain bulk geochemical data. An additional twenty-nine XRF data points from 2014-15 field deployments were included in the geochemical analysis. Samples were prepared by removing surface weathering using a rock saw and then powdered using a steel rock crusher and agate mill. During the powdering stage, the rock crusher and agate mill were cleaned between each sample using ethanol to mitigate contamination. The powdered samples were heated in a Katanax K2 Prime Fusion Machine with lithium metaborate to create fused glass discs, which were analyzed using the XRF PANalytical PW-2400 model at the University of Western Ontario to obtain major element geochemical data (SiO_2, TiO_2, Al_2O_3, Fe_2O_3, MnO, MgO, CaO, Na_2O, K_2O, and P_2O_5).

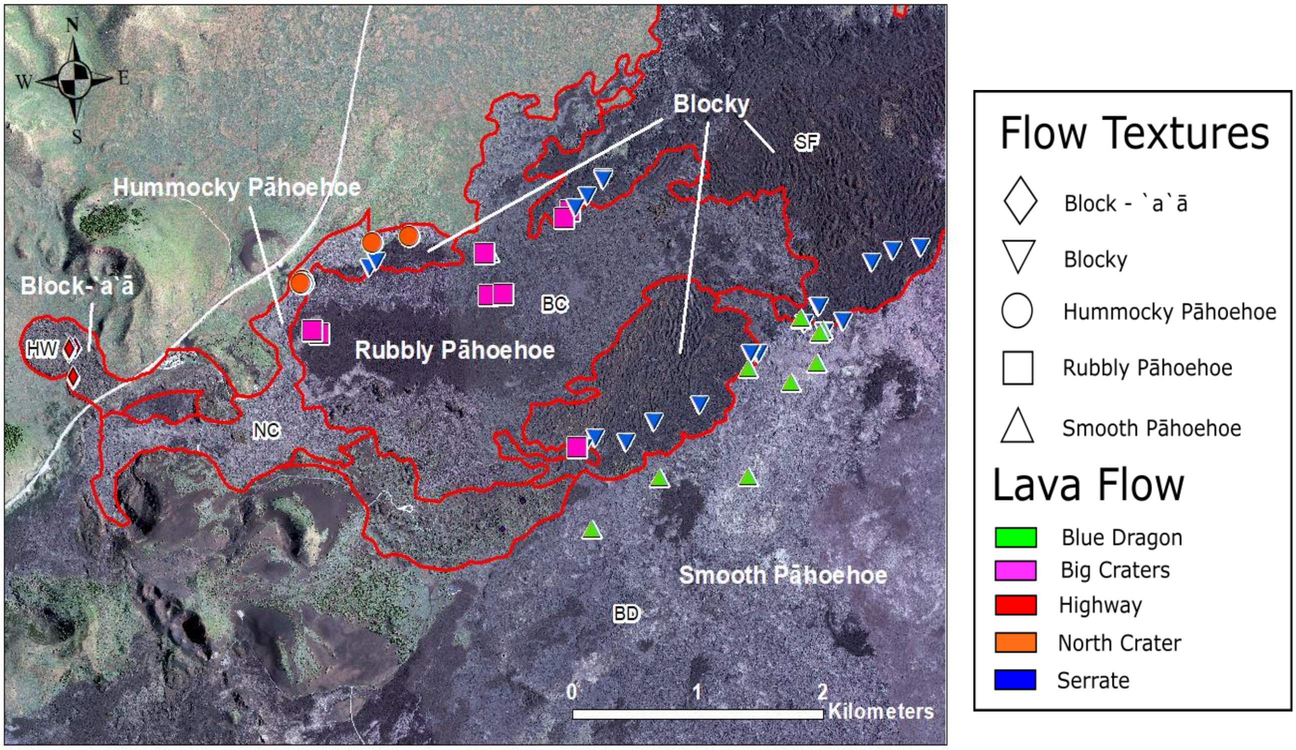

Figure 3. Field site at COTM. Symbols mark the locations of the 53 samples studied in this work. Red lines mark the lava flow margins from the Kuntz et al. (1989, 2007) geological map of COTM. The image was taken from NAIP data acquired in 2015. Labels of the lava flows provide a generalized surface roughness description (some flows show localized changes in surface roughness).

2.3 Surface roughness determination using radar datasets

To differentiate the surface roughness of lava flows remotely, we used previously processed Airborne Synthetic Aperture Radar (AIRSAR) L-Band (24 cm wavelength, 10 m/pixel resolution) datasets (Evans et al., 1986; Khan et al., 2007), which are sensitive to surface roughness at the decimetre scale (Carter et al., 2011; Neish and Carter, 2014). A low-flying aircraft collected the AIRSAR L-Band data in March 2003. We utilized circular polarization ratio (CPR) maps described in Neish et al. (2017) to quantify the surface roughness of the lava flows. A CPR value represents the ratio between the returned radar signal with the same circular polarization as transmitted (SC) to the returned signal with the opposite circular polarization (OC). Smooth surfaces produce single bounce backscatter, which flips the polarization of the radar signal returning more data in the opposite polarization. Rougher surfaces produce multiple-bounce backscatter returning an approximately equal number of OC and SC returns. Thus, low CPR (<0.5) indicates smooth surfaces, while moderate to high CPR (0.5-1) indicates rough surfaces. CPR values can exceed unity (>1) when double-bounce radar backscattering occurs on surfaces with natural corner reflectors, rock edges, and cracks (Campbell, 2012). Pāhoehoe flows typically have low (<0.5) CPR, \`a\`ā and transitional lava flows typically have moderate to high (0.5-<1.0) CPR, and blocky flows typically have CPR greater than one (Neish et al., 2017).

Radar signals also have the ability to penetrate the surface and scatter off subsurface interfaces and materials such as voids or clasts (Carter et al., 2011; Neish and Carter, 2014). To determine if the radar scattering was produced by surface scattering or subsurface interfaces, the degree of linear polarization (DLP) was also calculated. The DLP provides subsurface scattering information, which indicates the presence of material and/or lithological boundaries beneath the surface. When the circular polarized radar signal penetrates the surface, it changes to an elliptical signal, adding a linear component and therefore increasing the DLP. For example, a lithological contact is dominated by a quasi-specular subsurface scattering that returns high DLP (>0.3), while buried boulders are dominated by diffuse subsurface scattering that returns moderately high DLP (0.1 – 0.3) (Carter et al., 2011, 2006, 2004). Low values of DLP (<0.1) are consistent with subsurface layered materials where the dielectric constant only gradually increases with depth or lithological contacts are present that are deeper than the penetration depth (Carter et al., 2006). A combination of CPR and DLP is useful to understand the structure of the surface and subsurface of planetary surfaces. For example, low CP and high DLP indicates a smooth surface with a subsurface interface, while high CPR and low DLP indicates a rough surface with no subsurface interfaces (Neish and Carter, 2014).

The AIRSAR data has been made available in compressed Stokes matrix format, so we used the Stokes matrix (*W*) to calculate the DLP (Campbell, 2002).

$$DLP = |W_{12}|/W_{11} \quad \text{(Equation 1)}$$

W_{11} and W_{12} are elements in the Stokes matrix, W, which is a symmetrical real matrix representing the polarimetric backscatter properties of the SAR data (Zebker et al. 1990). To compare the radar data to the geochemical and petrographic results, we extracted mean CPR and DLP values from areas of the lava flows where samples were collected. To ensure the extracted mean CPR and DLP values are representative of the general surface roughness of the region, the resultant shape files covered multiple sample locations (not individual points). In addition, they did not include areas where vegetation and volcanic ash deposits were present. We then used the zonal statistics tool in ArcGIS to measure mean CPR and DLP and standard deviation for each representative area. From the sixty-seven samples, sixty, were within one of the representative areas.

3 Results

The six studied lava flows at COTM and their surface morphologies and roughness are shown in Figure 4. The descriptions of each lava flow are based on field observations; while lava flow morphologies vary somewhat across the flow, we are specifically interested in the dominant characteristics that are associated with the samples we collected. Blue Dragon is a smooth pāhoehoe lava flow with localized areas of inflated pāhoehoe crust and collapsed lava tube ceilings (Figure 4a). The lava flow name derives from its unique blue, titanium magnetite-rich crust (Faye and Miller, 1973).Serrate flow (Figure 4b) is a blocky latite lavas (Kuntz, 1989; Kuntz et al., 2007), composed of decimetre to metre-sized polyhedral blocks with smooth faces and dihedral angles. North Crater is a hummocky pāhoehoe lava flow with a faint blue colour similar to Blue Dragon (Figure 4c). Big Craters is a transitional lava flow with a rubbly pāhoehoe surface (Figure 4d). The rubbly surface is comprised of centimetre to decimetre-sized fragments of pāhoehoe crust, with no evidence of viscous disruption. Highway Flow, a latite, is described by Kuntz et al. (1988, 2007) as a blocky-`a`ā morphology, which is consistent with our field observations describing the surface as very jagged, sharp, and vesicular with conchoidal fracture features (Figure 4e).

3.1 Geochemical analysis

We categorized the lithology of each lava flow using the standard TAS volcanic classification (Na_2O + K_2O vs. SiO_2) scheme (Figure 5). A total of sixty-seven samples were studied. Twenty-nine of our sixty-seven samples were collected from 2014-15 field deployments. Figure 5 shows that each lava flow falls into one of two major categories with a few outliers: (1) basalt, trachybasalt, and basaltic trachyandesite, and (2) trachyandesite, and trachyte/trachydacite. The basalt and trachybasalt categories include the majority of the smooth, hummocky and rubbly pāhoehoe samples, although a few rubbly pāhoehoe samples plot as basaltic trachyandesite. Blocky and block-`a`ā lava flows have higher SiO_2 (>55 wt%) and alkali contents (7–10 wt%), classifying the lava flows as trachyandesite and trachyte/trachydacite. A few blocky samples plot as basaltic trachyandesite; these samples are randomly located in Serrate flows. Blocky and block-`a`ā flows are evolved, with relatively high SiO_2 (55–65 wt%), Na_2O (3.7–5.1 wt%) and K_2O (4.0–4.9 wt%) contents, and low TiO_2 (0.6–1.5 wt%), Fe_2O_3 (8.0–15.5 wt%), CaO (2.8–4.9 wt%), and MgO (0.2–1.3 wt%) (Figure 6). Primitive smooth, hummocky, and rubbly pāhoehoe flows are low in SiO_2 (48–52 wt%), Na_2O (2.75–4.3 wt%) and K_2O (1.9–2.3 wt%), and high in TiO_2 (2.5–3.05 wt%), Fe_2O_3 (15–17.7 wt%), CaO (6.3–7.2 wt%), and MgO (2.3–4.2 wt%) (Figure 6). Despite having an evolved composition, the blocky Serrate flows yielded a few samples that plot as a third group, between the primitive and evolved lava flows. We focus on SiO_2 in this study because it influences silicate melt properties (e.g., increased polymerization of the silicate network), which in turn influences the lava viscosity affecting the surface roughness (Lejeune and Richet, 1995; Campbell et al., 2009).

Figure 4. Lava flow morphologies and textures observed and studied at COTM (symbols in top right corners represent the flow texture): **(a)** Smooth pāhoehoe texture at the Blue Dragon lava flow in the southern region of the field site (triangle). **(b)** Blocky textures at the Serrate lava flow; image was taken close to the Serrate lava flow margin (triangle_down). **(c)** Hummocky pāhoehoe textures at the North Crater lava flow with the distinctive blue colouring on its surface (circle). **(d)** Big Craters lava flow with a rubbly pāhoehoe surface (square). **(e)** Blocky to \`a\`ā textures at the Highway flow (diamond).

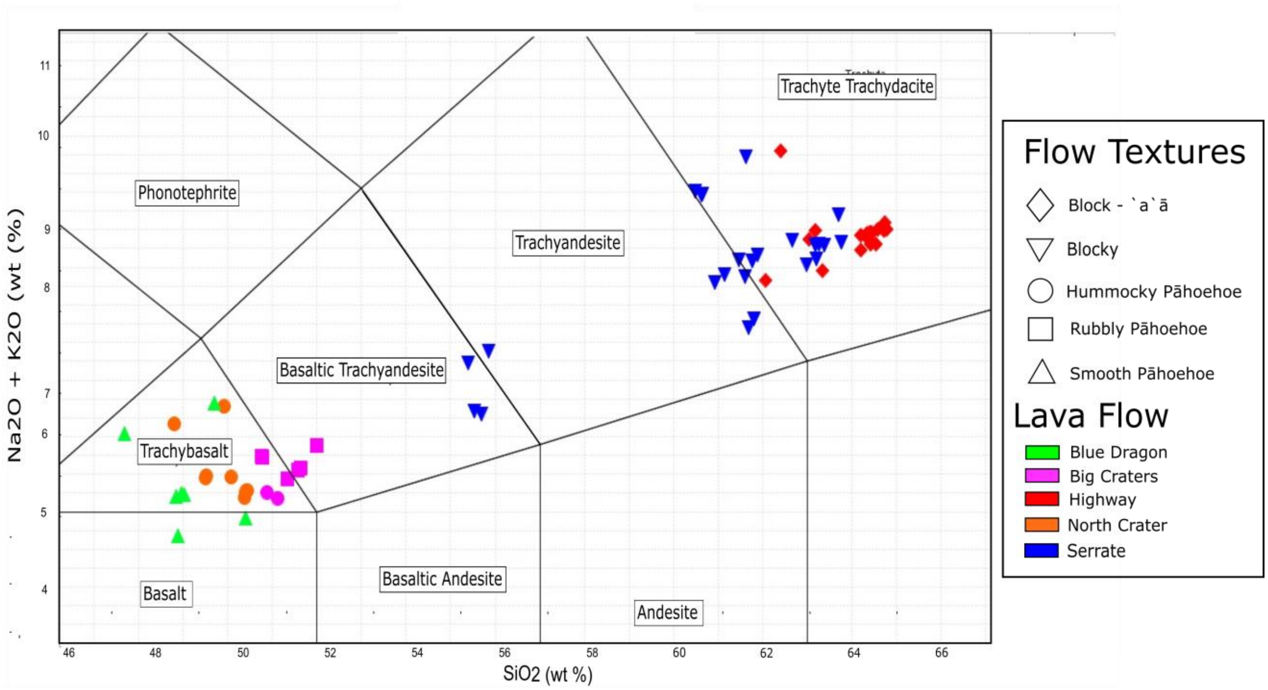

Figure 5. Volcanic Total Alkali Silica (TAS) diagram comparing COTM lava flows from our study area using alkali (Na_2O+K_2O) and silica (SiO_2) compositions. COTM lavas show a range of volcanic types from basalt to trachyte/trachydacite.

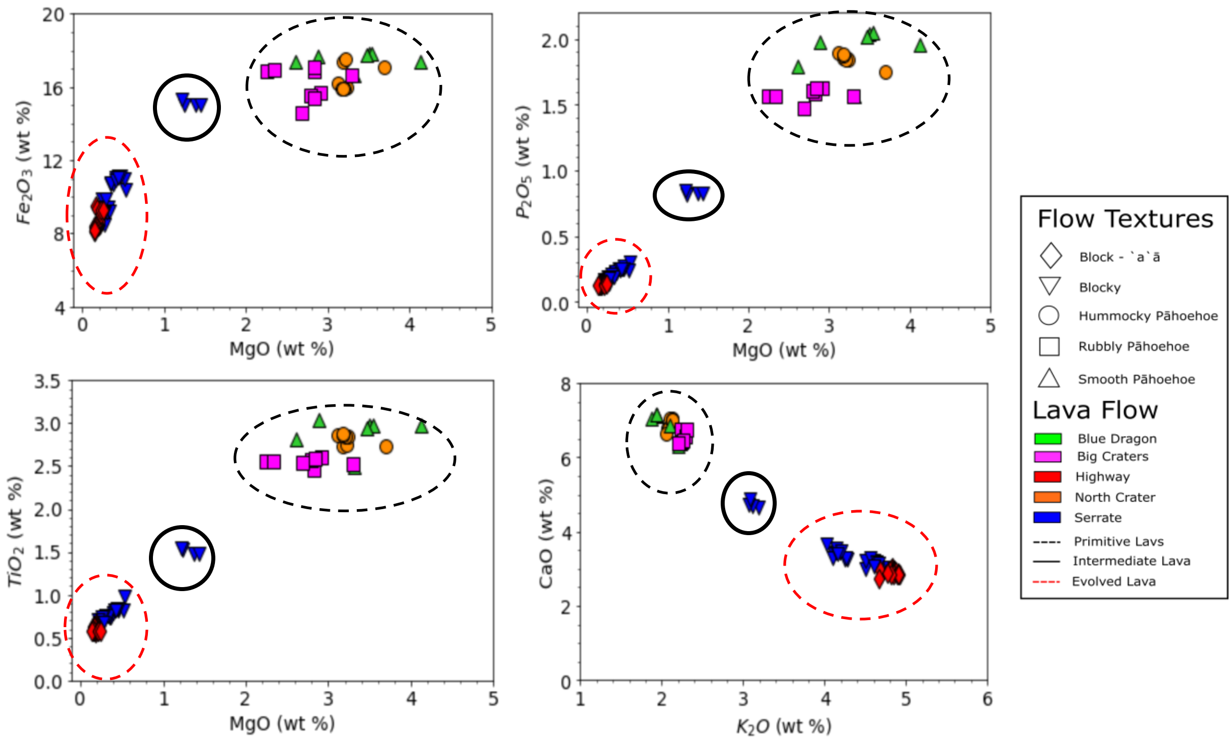

Figure 6. Major element XRF data from COTM. Oxides of Mg, Fe, P, Ti, K and Ca plotted to show the similarities and diversity between composition and surface roughness. The surface roughness described in the field are clustered as two separate groups, with a few data points from the blocky lava flows (Serrate) plotted in an intermediate zone. Black dashed outlines highlight the primitive lava compositions, red dash outlines highlight the more evolved lava compositions, and the solid black circle highlights samples with intermediate compositions. Legend above applies to all of the graphs.

3.2 Petrographic analysis

The primitive lava flows exhibit similar mineralogical and petrographic properties, with elongate and partially tabular plagioclase crystals (0.1–0.2 mm, 32–55 vol%) and fine-grained anhedral to subhedral fayalite and augite crystals (0.05–0.1 mm, 4–15 vol%) (Figure 7a-b). The crystals are all encased within a quenched, black, opaque glass matrix. The lava flows all contain large vesicles, some reaching diameters >1 cm, with most within the range of 0.1–0.5 cm. Larger vesicles reaching sizes >5 cm were observed in the field (summarized in Table 2).

Plagioclase crystals in the hummocky and rubbly pāhoehoe flows become oriented sub-parallel to the local flow direction further from the volcanic vent (Figure 7c). Along with the orientation, the average plagioclase crystal size slightly decreases from 0.2 mm to 0.1–0.05 mm. The amount of black, opaque glass matrix also decreases with distance from the lava flow source. Crystallinity increases from ~40% at the vents to 60% at a down-flow distance of 1.6 km (Table 2). Distinct orientation of plagioclase crystals is not observed in most smooth pāhoehoe samples, but the plagioclase crystals are 0.5–1 mm larger than the crystals in hummocky and rubbly pāhoehoe. When plagioclase orientation is present however, it is not well defined. The orientation of plagioclase crystals and change in crystallinity shows a transition from hypocrystalline to trachytic textures with distance from vent. The smooth pāhoehoe lava flow does not show changes in petrographic texture. The lava flow maintained a hypocrystalline texture, except close to the flow margins where cooling was slightly faster and produced a more glass-rich texture. The textural changes observed in rubbly pāhoehoe flow was not associated with a change in surface roughness, unlike the hummocky pāhoehoe, though both flows were geochemically and petrographically similar (Figure 6 and 7b+c).

Sample No.	Lava Flow	Coordinates	Surface Roughness	Textures	Pl (%)	Ol (%)	Cpx (%)	Op (%)	Ano (%)	Ap (%)	Glass (%)	Crystallinity (%)	Vesicles (%)
COTM16009	Big Craters	43°28'0.76"N, 113°32'53.37"W	Rubbly Pāhoehoe	Hypocrystalline-Trachytic	30	10	5	2	-	Trace	52	47	30
COTM16011	Big Craters	43°27'48.48"N, 113°32'48.61"W	Rubbly Pāhoehoe	Hypocrystalline-Trachytic	40	5	3	2	-	Trace	50	50	30
COTM16012	Big Craters	43°27'49.35"N, 113°32'50.87"W	Rubbly Pāhoehoe	Hypocrystalline	40	10	5	7	-	Trace	38	62	50
COTM16031	Big Craters	43°28'4.65"N, 113°32'30.96"W	Rubbly Pāhoehoe	Hypocrystalline	50	2	1	2	-	-	45	55	50
COTM16034	Big Craters	43°27'56.02"N, 113°31'42.78"W	Rubbly Pāhoehoe	Trachytic	55	5	5	3	-	2	30	70	40
COTM16035	Big Craters	43°28'15.33"N, 113°31'17.86"W	Rubbly Pāhoehoe	Trachytic	50	3	2	2	1	Trace	42	58	55
COTM16036	Big Craters	43°28'13.62"N, 113°31'20.39"W	Hummocky Pāhoehoe	Trachytic	40	5	2	2	-	1	50	50	20
COTM16001	Blue Dragon	43°27'46.74"N, 113°29'57.68"W	Smooth Pāhoehoe	Hypocrystalline	50	3	1	4	1	1	40	60	40
COTM16007	Blue Dragon	43°27'35.52"N, 113°30'16.86"W	Smooth Pāhoehoe	Hypocrystalline	32	3	1	3	-	1	60	40	20
COTM16016	Blue Dragon	43°27'43.12"N, 113°29'51.00"W	Smooth Pāhoehoe	Hypocrystalline	45	10	3	4	1	-	37	63	35
COTM16020	Blue Dragon	43°27'50.46"N, 113°29'52.47"W	Hummocky Pāhoehoe	Hypocrystalline	40	5	5	4	-	Trace	46	54	40
COTM16027	Blue Dragon	43°27'19.31"N, 113°31'17.54"W	Hummocky Pāhoehoe	Hypocrystalline	39	5	3	3	-	Trace	50	50	30
COTM16033	Blue Dragon	43°28'6.01"N, 113°31'47.31"W	Hummocky Pāhoehoe	Hypocrystalline	45	3	3	3	-	2	44	56	30
HF16001	Highway Flow	43°27'48.01"N, 113°34'16.90"W	Blocky – `a`ā	Holohyaline	-	-	-	-	-	-	100	0	80
HF16002	Highway Flow	43°27'48.06"N, 113°34'16.89"W	Blocky – `a`ā	Holohyaline	2	-	-	-	-	-	98	2	>80
HF16003	Highway Flow	43°27'47.82"N, 113°34'17.26"W	Blocky – `a`ā	Holocrystalline	55	3	5	1	2	2	32	68	50
HF16004	Highway Flow	43°27'47.75"N, 113°34'17.33"W	Blocky – `a`ā	Vitrophyric - Holohyaline	-	-	-	-	-	-	95	5	65
COTM16010	North Crater	43°28'0.91"N, 113°32'54.46"W	Smooth Pāhoehoe	Hypocrystalline	50	5	5	3	-	-	37	63	20
COTM16013	Serrate Flow	43°27'44.79"N, 113°29'50.85"W	Blocky	Trachytic	50	3	3	2	2	Trace	40	60	45
COTM16014	Serrate Flow	43°27'44.37"N, 113°29'50.72"W	Blocky	Trachytic	50	3	1	4	2	-	40	60	50
COTM16017	Serrate Flow	43°27'47.83"N, 113°29'43.84"W	Blocky	Trachytic	50	3	1	3	1	-	42	58	80
COTM16018	Serrate Flow	43°27'50.73"N, 113°29'52.48"W	Blocky	Trachytic	50	10	3	5	-	-	32	68	60
COTM16019	Serrate Flow	43°27'50.68"N, 113°29'52.00"W	Blocky	Trachytic	50	10	5	4	-	-	31	69	20

Table 2. Mineral modes, textures, and vesicularity of thin section samples from COTM lava flows. The table summarizes the texture and mineralogy in the lava flow samples. Opaque's (Op) comprises ülvospinel and magnetite crystals. Mineral abbreviations: Olivine (Ol), clinopyroxene (Cpx), apatite (Ap), plagioclase (Pl), and anorthoclase (Ano).

The chemically evolved blocky lava flows exhibit more crystal orientation than the less evolved lava flows and have a finer grained (<50 µm to 1 mm) groundmass. Plagioclase crystals are slightly more acicular than tabular. Subhedral to anhedral fayalite and augite crystals ranging in size from 0.05–1 mm are encased in a deep brown volcanic glass matrix. Also, within the glass matrix are vesicles with an average diameter of 0.5 mm with some larger vesicles >1 cm in diameter.

Crystallinity in the evolved lava flows is greater than the primitive lava flows (60–70% vs 40–60%). Close to the volcanic vent, the blocky flows exhibit aphanitic textures (Figure 7d) that transition to micro-trachytic textures. The glass content remains unchanged during this transition, remaining between 35–40%. Progressing further from the vent the texture becomes more trachytic, with slightly coarser (increasing from <50 µm–1 mm to 0.5 mm–1.5 mm) and more oriented plagioclase crystals.

The Highway block-`a`ā lava flow, although classed as evolved lava, exhibits different petrographic properties. The vesicularity ranges from ~30% to >80% in localized patches in the field. The surface has a holohyaline texture, with very fine-grained crystals that are not observable under optical microscopy, is very vesicular (Figure 7e), and comprises a deep orange glass matrix. The interior of the flow, however, is porphyritic (Figure 7f).

A closer investigation of the black opaque and deep brown glass matrix using BSE imagery revealed an array of quench textures. In the black glass, skeletal fayalite nucleated around the margins of the elongate and partially tabular plagioclase crystals (Figure 8a). Augite crystals grew around the tips of the plagioclase, creating a feathered texture. In the deep brown glass, the quenched textures are not as well defined. Skeletal fayalite and feathered augite are not as abundant, and most of the matrix is composed of single quenched glass matrix with no microlites (Figure 8b).

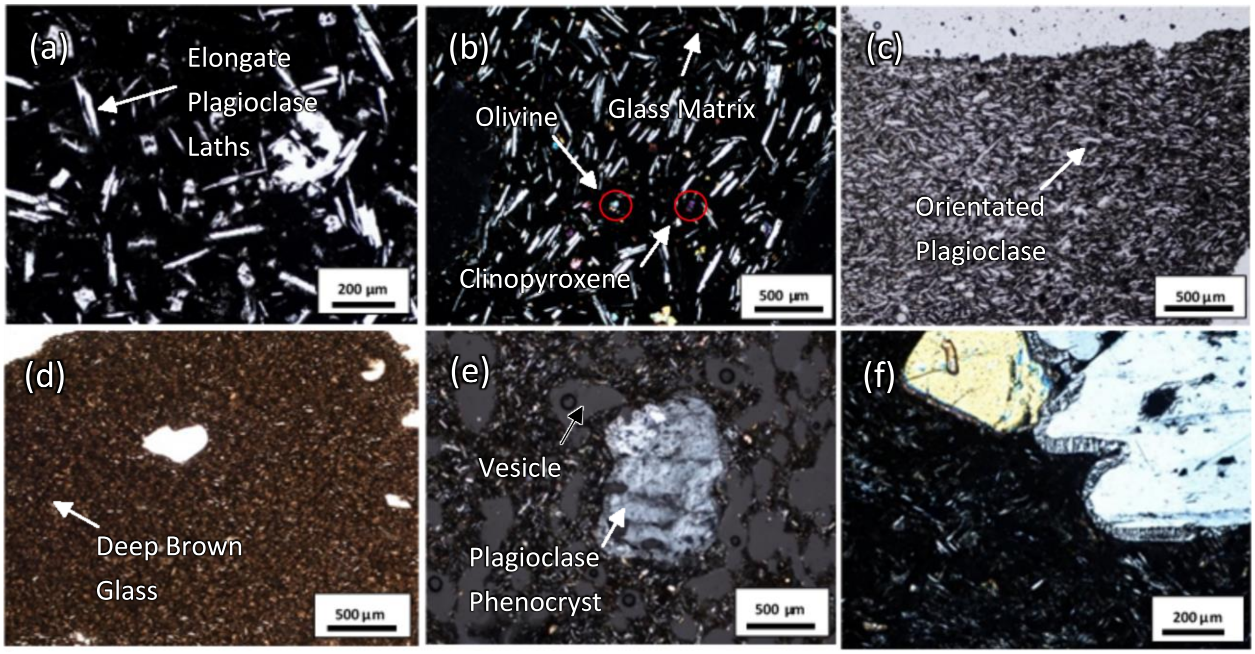

Figure 7. Petrographic images from COTM lava flows. (a) Elongate plagioclase laths encased in volcanic glass from smooth pāhoehoe Blue Dragon flow. (b) Black opaque glass matrix encasing elongate plagioclase, subhedral clinopyroxene, and fine-grained olivine crystals from rubbly pāhoehoe Big Craters (red circles highlight olivine and clinopyroxene crystals). (c) Elongate plagioclase crystals are orientated sub-parallel to the lava flow direction. Sample is from Big Craters flow. (d) Deep brown glass matrix in an aphanitic texture. Sample is from the blocky flow. (e) Plagioclase phenocryst with partially consumed crystal margins. Sample is from blocky to \`a\`ā Highway flow. (f) Porphyritic texture with olivine and plagioclase phenocrysts with no zonation patterns. Sample is from blocky to \`a\`ā Highway flow.

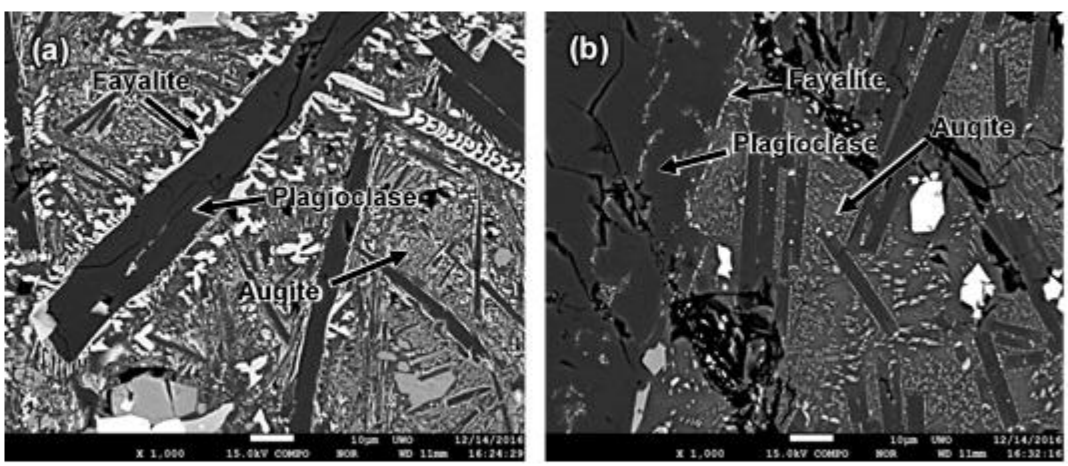

Figure 8. Quenched skeletal fayalite and feather-like augite observed using backscatter electron (BSE) imagery. Augite crystallized on the margins of the elongate tabular plagioclase crystals. The textures in the left image (a) are from lava flows with smooth and rubbly pāhoehoe samples (primitive), and the right image (b) are from blocky lava flows (evolved).

3.3 Radar properties

Ten polygons were traced on the AIRSAR L-band dataset over areas where thirty of the fifty-three samples were collected. These were used to calculate the mean and standard deviation CPR, which is representative of the surface roughness of the associated lava flow (Table 3). The size of all the polygons are not uniform because they were traced to fit clustered samples, and avoid vegetation, degraded lava surfaces and volcanic ash deposits. A low pass filter was applied to the AIRSAR L-Band dataset to reduce the speckle noise in the image, which scales as $1/N^{1/2}$, where N is the number of looks in each pixel. The low pass filter averaged the CPR over a 3x3 pixel area, increasing the number of looks per pixel from 9 to 81 (hence reducing the speckle noise from 33% to 11%). The zonal statistics tool in ArcGIS was applied after filtering to calculate the mean CPR for each region of interest (Table 3). The smooth pāhoehoe surface returned values of 0.34 ± 0.11, consistent with single bounce backscattering (quasi-specular). The blocky surfaces returned values between 0.91–1.14 ± 0.19–0.2, consistent with double bounce backscattering (Neish and Carter, 2014). The block-`a`ā lava flow returned a value of 0.69 ± 0.25, almost identical to the rubbly pāhoehoe flow, 0.73 ± 0.24, and is consistent with multiple bounce backscattering (diffuse). The "Humm_Blocky" polygon is not its own lava flow but the rubbly and smooth pāhoehoe flows overlying a blocky flow (Figure 9). The polygon's mean CPR value (0.65 ± 0.34) is less than the block-`a`ā and rubbly pāhoehoe but greater than the hummocky pāhoehoe surface from North Crater (0.48 ± 0.19) and Big Craters (0.56 ± 0.21). The large standard deviation calculated from the Humm_Blocky polygon is likely due to the presence of two different surface roughness textures in this region (Section 4.2, Figure 11).

In addition to surface scattering, radar has the capability to penetrate through the surface to any underlying clasts, voids, or interfaces (e.g., lithological contacts). The penetration depth (d) of a radar signal is dependent on the illumination wavelength (λ), the loss tangent of the substrate ($\tan\delta$), and its real dielectric constant (ε') (Equation 2).

$$d = \lambda / (2\pi\sqrt{(\varepsilon')}\tan\delta) \qquad \text{(Equation 2)}$$

For example, Neish et al. (2014) calculated the penetration depth of a 19 cm radar signal into lunar impact melt flows (estimated 2.5 g/cm^3 density) to be within a range of 20–500 cm (calculated using dielectric constant values from Ulaby et al. (1988)). Basaltic lava flows exhibit a bulk density of 3 g/cm^3. Using real ($\varepsilon' = 1.96^{\rho(3\text{-}3.3)}$) and imaginary ($\varepsilon''$) dielectric constant values from volcanic rocks within this density range (ε'' = 0.11–0.18 from Ulaby et al. (1988)) we calculated the loss tangent ($\tan\delta = \varepsilon''/\varepsilon'$). With these values, we calculated a penetration depth for the 24 cm L-band radar from 60–100 cm. Since the penetration depth is no larger than a metre we would not expect much subsurface scattering in the AIRSAR data within the COTM field site.

In order to determine if the radar returns were the result of surface or subsurface scattering, we calculated the DLP of the lava flows (Neish and Carter, 2014) using the Stokes Matrix (Section 2.3, Equation 1). A lowpass filter was applied to the DLP dataset to reduce speckle noise, and quantified values were calculated using zonal statistics. The lava flows returned low DLP values of 0.18 – 0.2 ± 0.05 – 0.06 (Table 3), compared to areas in the northern and western part of the field site, which returned DLP values of 0.25 ± 0.06 (Figure 10). These regions of higher DLP are covered in ash deposits, where one would expect more subsurface scattering from buried lava flows. In our study area, the smooth pāhoehoe lava flow has a mean CPR of 0.34 and mean DLP of 0.18. With a low CPR and DLP, this suggests a smooth surface with little subsurface scattering (Carter et al., 2011). The rest of the lava flows exhibit moderate to high CPR and low DLP. This suggests a rough surface with little subsurface scattering.

Polygon Raster ID	Surface Roughness	Lava Flow	CPR	CPR STD	DLP	STD
Block_`a`ā (1)	Block-`a`ā	Highway Flow	0.69	0.25	0.20	0.06
Blocky_1 (2)	Blocky	Serrate	1.1	0.35	0.20	0.05
Blocky_2 (3)	Blocky	Serrate	0.91	0.30	0.19	0.05
Blocky_3 (4)	Blocky	Serrate	1.05	0.34	0.20	0.06
Blocky_4 (5)	Blocky	Serrate	1.14	0.32	0.19	0.05
Hummocky_Pāhoehoe_1 (6)	Hummocky	Big Craters	0.56	0.21	0.18	0.05
Hummocky_Pāhoehoe_2 (7)	Hummocky	North Crater	0.48	0.19	0.20	0.06
Humm_Blocky (8)	Hummocky over Blocky	Blue Dragon covering Serrate	0.65	0.34	0.19	0.05
Rubbly_Pāhoehoe (9)	Rubbly	Big Craters	0.73	0.24	0.19	0.05
Smooth_Pāhoehoe (10)	Smooth Pāhoehoe	Blue Dragon	0.34	0.11	0.18	0.05

Table 3. The above table contains the CPR, standard deviation and DLP values of the traced lava flow polygons (bracketed numbers are the polygon labels, see figures 9 and 10). The polygons covered areas of the lava flows where samples were collected to allow for comparisons between the remote sensing, geochemical, and petrographical data. CPR values show differences and similarities between the surface roughness descriptions but DLP remains relatively homogeneous at 0.18–0.20.

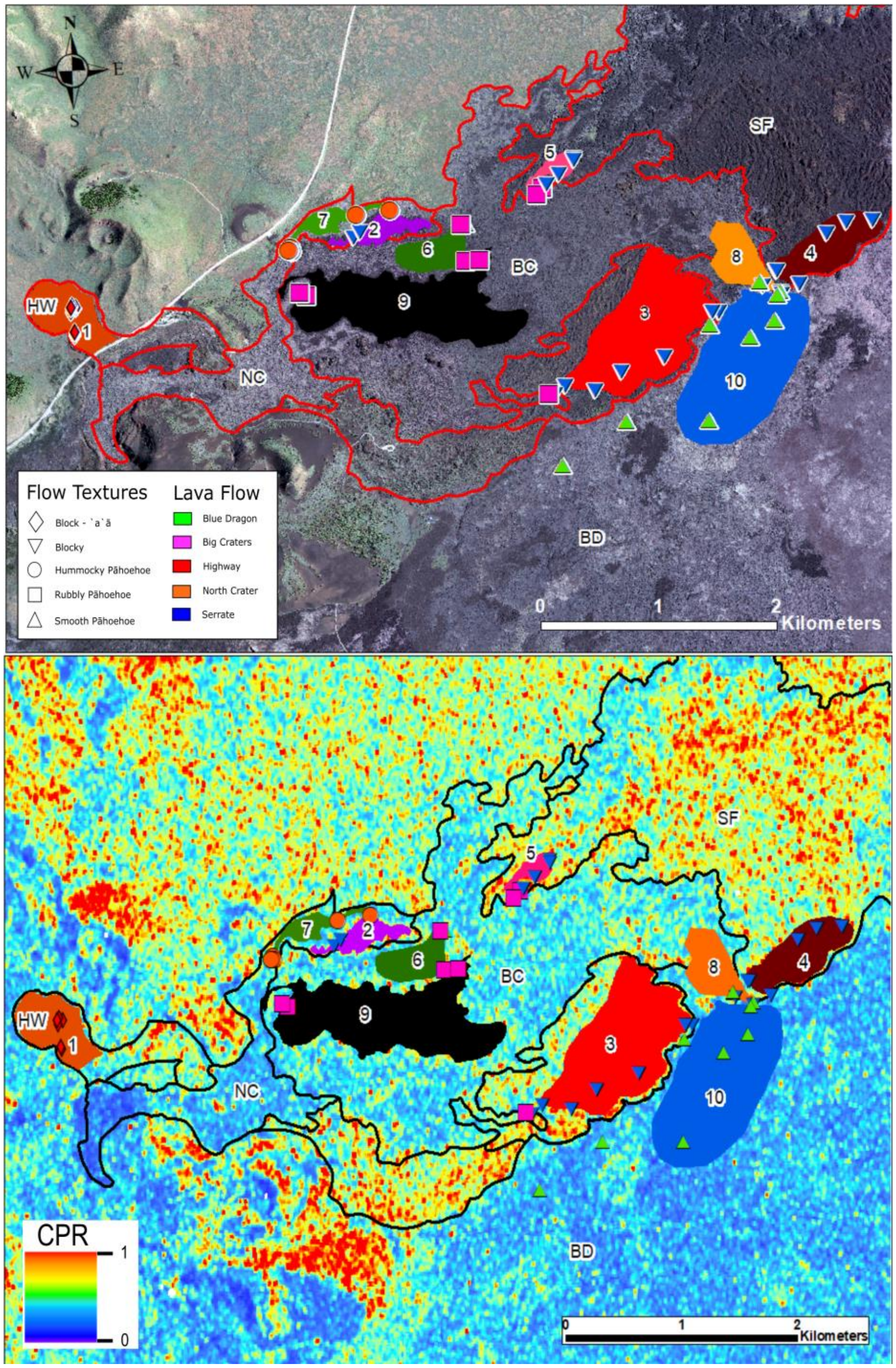

Figure 9. The AIRSAR data covering the COTM field site. Locations of lava flow shape files traced in ArcGIS, overlain on a NAIP visual image with lava flow margins marked with red lines (top). Sample locations are indicated by white symbols (see Figure 3). AIRSAR CPR data set (~12 m/pixel) after a 3x3 lowpass filter has been applied (bottom). The CPR values within each polygon raster were averaged using zonal statistics. Some samples were not incorporated because they are in areas with vegetation and volcanic ash deposits.

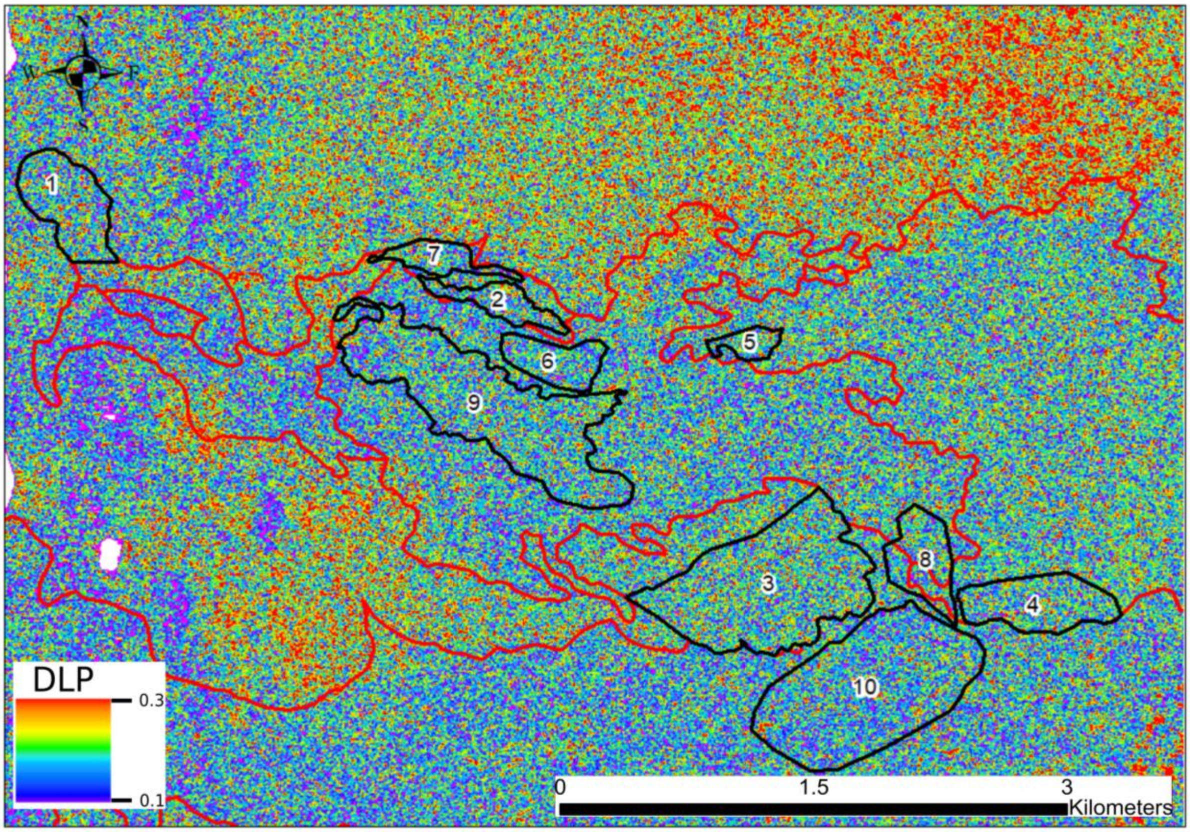

Figure 10. Degree of linear polarization (DLP) pixels calculated from AIRSAR L-band data. Lava flow margins are marked with red lines, and shape files are marked with black lines. The lava flows show low DLP values indicating little backscatter from subsurface interfaces and material. Red-orange areas (≥0.3) represent ash deposits, lapilli, and aeolian sediments. Their greater values are most likely indicating subsurface scattering from older buried lava flows.

4 Discussion

Lava flows on Earth and other planetary surfaces can exhibit similar surface morphologies when analysed using remote sensing data (Campbell and Shepard, 1996; Campbell et al., 2010; Harmon et al., 2012; Neish et al., 2017), making it difficult to infer their differing lava properties and emplacement processes. To help address this issue, the overarching goal of this study was to investigate whether there was any correlation between the geochemistry, petrography, and radar data of a diverse range of lava flows at COTM. This will allow us to understand the extent to which we can predict the lava properties and emplacement processes of a lava flow using only a remotely derived measure of decimetre scale roughness.

4.1 Radar statistics compared to surface morphology

Our results show that the blocky lava flows returned CPR values reaching and exceeding unity while the smooth, hummocky and rubbly pāhoehoe lava flows returned values <0.75. The smooth pāhoehoe surfaces have a CPR of 0.34 ± 0.11, indicative of single bounce backscattering, common for smooth surfaces. The blocky surfaces returned values between 0.91–1.14 (±0.25–0.35), suggestive of double bounce backscattering from natural corner reflectors. The rubbly pāhoehoe surfaces have a CPR of 0.73 ± 0.24, which implies the surface scattered the radar signal in multiple directions (diffuse scattering). The hummocky flow overlying the blocky flows also returned similar CPR values, 0.65 ± 0.34 ("Humm_Blocky" in Figure 10). Even though this does not represent an individual flow, it may be difficult to distinguish rough lava flows from smooth lava flows overlying older rougher lava flows in remote sensing data. The block-\`a\`ā flow has a CPR of 0.69 ± 0.25, which is also similar to the rubbly pāhoehoe. The block-\`a\`ā lava flow was anticipated to return a CPR value greater than the rubbly pāhoehoe flow because of its jagged, sharp, vesicular surface, and conchoidal fracture features. However, the surface of the block-\`a\`ā flow must lack the natural corner reflectors required for double bounce backscattering. Thus, when observed with L-band radar (Figure 9), the block-\`a\`ā and rubbly pāhoehoe lava flows appear analogous. It would be difficult to distinguish them as different surface morphologies without in situ data. Hawaiian \`a\`ā lava flows also have CPR values similar to rubbly pāhoehoe (Campbell, 2002) complicating the matter further.

In addition, our results show that lava flows exhibiting similar CPR values also have contrasting petrographic textures. The rubbly pāhoehoe transitions from holocrystalline to trachytic textures while the block-`a`ā exhibits holohyaline and porphyritic textures. It is not surprising that these two lava flows exhibit different petrographic textures since both formed under different processes. The rubbly pāhoehoe formed via mechanical fracturing of a quenched pāhoehoe crust while the block-`a`ā flowed over the surface in a creeping-motion in response to its high SiO_2 and viscosity, and an increase in rate of shear. On the other hand, the rubbly pāhoehoe and hummocky pāhoehoe lava flows are easily distinguishable in the field and in the radar data (Figure 9). Their geochemistry and petrography, however, are indistinguishable, both exhibiting similar major elemental content (Figure 5 and 6, Section 3.1), and hypocrystalline and trachytic textures (Table 3, Section 3.2).

Without ground-truth information, our interpretations of the lava flow properties and emplacement processes using radar data are therefore limited. However, the diverse surface roughness and morphology of the studied COTM lava flows provides a wide selection of examples to compare to lava flows in other volcanic regions on Earth and other planetary surfaces, aiding in our understanding of their origin and emplacement.

4.2 Radar statistics compared to SiO_2 content

The SiO_2 of the lava flows varies across the northern area of COTM (45–65 wt%). With such a wide variation in SiO_2 content, and with composition being a property that influences surface morphology and roughness, we might expect to observe some correlation between SiO_2 and the CPR values. To test this hypothesis, we plotted SiO_2 versus mean CPR for each lava flow studied (Figure 11). Only samples that were within the boundaries of the polygons traced in Figure 9 were included in this plot. Using Pearson's correlation coefficient, we calculated the strength of the relationship between SiO_2 and CPR. Pearson's correlation coefficient formula determines whether a correlation exists between two variables (Egghe and Rousseau, 1990). A positive correlation will return values ≥0.5–1 while a negative correlation will return values ≤-0.5

– -1. Coefficient values close or equal to zero indicate a weak or non-existent correlation between the variables. A calculated value of 0.63 indicates the CPR and SiO_2 have a positive correlation. However, we observed some exceptions to this correlation. The smooth, hummocky and rubbly pāhoehoe lava flows showed an increase in CPR as expected, but the SiO_2 did not change. This is because the rubbly pāhoehoe surface forms from mechanical fracturing, rather than viscosity changes related to increasing SiO_2. The block-`a`ā flow also does not follow the upward trend in CPR with SiO_2. Although it is as siliceous as the blocky flows, the block-`a`ā lacks natural corner reflectors on its surface so it is unable to return CPR values above unity. The emplacement of the block-`a`ā flow may be more akin to an `a`ā flow than a blocky flow and may have not been emplaced under the creep fracturing movement associated with blocky lava eruptions (MacDonald, 1953). In addition to the similarity between the block-`a`ā and rubbly pāhoehoe lava flow, the standard deviations of most of the studied COTM lava flows overlap. Without ground-truth information to confirm the surface morphology and roughness, most lava flows could be misidentified using radar remote sensing data. Clear distinctions however can be made between smooth pāhoehoe and blocky lava flows as the data does not overlap. Smooth and very rough lava flows can easily be distinguished, however intermediate rough (e.g., block-`a`ā and rubbly) lava flows will present more difficulty.

From the data, we observe a general increase in CPR with silica content, if this correlation was applied to interpret the surface morphology and roughness of lava flows on other planetary surfaces, incorrect interpretations could arise. Highly siliceous lava flows will not always return high CPR values if they lack the natural corner reflectors necessary for double bounce backscattering. They would appear indistinguishable to transitional lava flows such as rubbly pāhoehoe flows or Hawaiian `a`ā flows (Campbell, 2002). Similarly, lava flows with lower silica content that have been mechanically fractured will show an increase in CPR unrelated to their composition, as we see for the rubbly pāhoehoe at COTM.

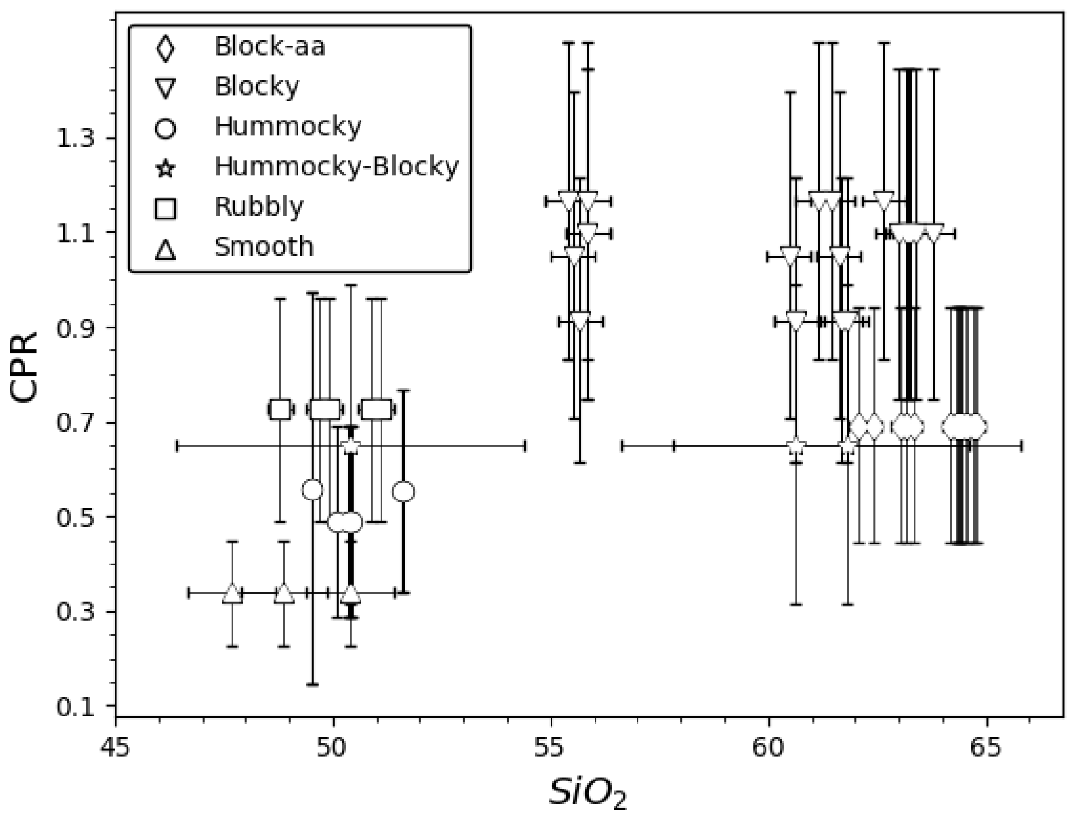

Figure 11. CPR vs SiO_2 content for each lava flow type studied in this work, including our data collected from field deployments in 2014 and 2015. The data points represent the different surface roughness descriptions of the lava flows. Number of data points: Block-`a`ā (18), blocky (22), hummocky (9), hummocky-blocky (3), rubbly (5), and smooth (3).

4.3 Using radar statistics to reconstruct lava emplacement mechanisms

To infer lava properties and emplacement processes on other planetary surfaces and remote locations on Earth where fieldwork is not possible, we must rely on morphological and surface roughness studies from remote sensing data sets (Campbell, 2012; Campbell et al., 2010, 2009; Carter et al., 2006; Harmon et al., 2012; Morgan et al., 2016; Patterson et al., 2017; Shepard et al., 2001). From our results, we show that radar data cannot always distinguish lava flows with different surface morphologies. The similar mean CPR values from the block-`a`ā and rubbly pāhoehoe flow would lead to ambiguous interpretations about their emplacement conditions and lava properties if one were to rely on radar data alone. The difference in CPR between the siliceous blocky and block-`a`ā demonstrates that not all siliceous lava flows exhibit double-bounce backscattering and return CPR values ≥1.0. In some cases, visible imagery might be able to distinguish the lava flows and aid in interpreting the emplacement styles, but only if the resolution is high enough. For example, in high-resolution (1 m/pixel) optical images, the hummocky pāhoehoe flow can be seen covering the blocky flows, providing evidence that it is a younger flow overlying an older, rougher flow. In many instances though, such high-resolution imagery is not publicly available, or its scale is too coarse to highlight centimetre - decimetre scale roughness differences. In planetary science, the highest-resolution optical data available, notably the 0.25 m/pixel HiRISE instrument on the Mars Reconnaissance Orbiter (McEwen et al., 2007) and the 0.5 m/pixel Lunar Reconnaissance Orbiter Camera instrument (Chin et al., 2007) can observe some surface features such as metre-sized pāhoehoe slabs. However, surface features such as clinkered `a`ā and rubbly pāhoehoe cannot be observed.

As a result, CPR coupled with high-resolution optical imagery is insufficient to differentiate all lava surfaces at our study site in COTM. Without ground-truth information (field observations, and geochemical and petrographic data), misinterpretations about the lava properties and emplacement processes of the COTM lava flows would have been made. The lava flows may have been presumed to be emplaced under similar conditions, leading to false interpretations about their volcanic eruption history and magmatic origin. However, the use of radar for understanding lava flow emplacement and properties should not be disregarded because of these results. In fact, a general trend of increasing in CPR with increasing SiO_2 is observed. Instead, we suggest that caution needs to be taken when interpreting remote sensing data. For example, a study by Kolzenburg et al. (2018) raises the concern that rheological inferences on lava flows using remote sensing data may be over exaggerated because inflation after the cessation of flow-front advance may continue to change the surface morphology and roughness. However, with no magma flux, lava flow morphology is unlikely to change, with the exception of mechanical fracturing of surfaces due to lava drainage.

Note that the AIRSAR data was at 24 cm wavelength and is only sensitive to surface features of that scale. Smaller radar wavelengths such as C-Band (5.6 cm wavelength) may have revealed different discrepancies between the lava flow surfaces if centimetre scale features were detected. The same would apply if longer radar wavelengths (e.g. P-Band, 70 cm) were used. L-Band data was used in this study because it best discriminated the lava flow surface roughness types at COTM (Zanetti et al., 2018).

In summary, radar remote sensing data provides important information about lava flow emplacement, but still has its limitations and ambiguities, especially when studying lava flows on other planetary surfaces where ground-truth information is not available. Until extensive ground-truth data becomes available for planetary bodies, when interpreting radar data, we should consider multiple lava flow types that can produce a common CPR value. For example, Arecibo P-band CPR data of Mare Imbrium lava flows are similar to CPR values for terrestrial lava flows (Campbell et al., 2007; Morgan et al., 2016). Radar bright mare flows with a CPR of 0.6 match values for terrestrial `a`ā, hummocky, and slabby pāhoehoe at L-Band. These wavelengths differ by more than a factor of two (24 cm vs. 70 cm) and the SAR spatial resolutions differ drastically (12 m/pixel vs. 200 m/pixel), so we cannot exactly compare the results. The P-band data will be sensitive to roughness at a slightly larger scale than that of the L-band data. Lava flows at Mare Serenitatis and Mare Crisium may exhibit CPR values similar to Mare Imbrium and COTM. Additional work could investigate the roughness of lava flows from other lunar maria, including Eratosthenian-aged lava flows in the S-SW region of Mare Imbrium with analogous flow and surface morphology to flood basalts (Schaber, 1973).

Most lunar maria are proposed to have formed from the development and growth of compound lava flows, with multiple layers of lava flows stacking around the eruption source (Head and Wilson, 2017). The compound lava flow deposits formed from moderate effusion rate (10^4 – 10^6 m^3 s^{-1}) eruptions emplacing cooling-limited flows (Head and Wilson, 2017). These compound lava flows are most analogous to the basalt plain volcanic setting at COTM since they comprise multilayered flows, with flow concentrations adjacent to the vents. With such a wide range of potential surface morphologies on the Moon, only in-situ measurements can provide clarification regarding their emplacement style. Until future missions return to the Moon to provide ground truth information about the mare lava flows, more than one type of surface morphology could explain the radar remote sensing data.

5 Conclusions

The goal of this work was to establish a relationship between the geochemistry, petrography, and surface morphology/roughness of lava flows to improve predictions on their lava properties and emplacement processes using remote sensing data. Geochemically the lava flows were divisible into two major groups and one intermediate group. Each lava flow exhibited a variety of petrographic textures from hypocrystalline, porphyritic, aphanitic, trachytic, and holohyaline. The COTM lava flows exhibit a range of morphologies including smooth, hummocky and rubbly pāhoehoe, block-`a`ā, and blocky flows. The AIRSAR L-Band data revealed that rubbly pāhoehoe and block-`a`ā lava flows exhibit similar CPR values, making them appear almost indistinguishable in AIRSAR data. If ground-truth information were not obtained both lava flows could have been interpreted to be the same type of flow, which would have led to ambiguous interpretations about their emplacement and lava properties. Lava flows with different surface morphologies that exhibit similar mean CPR values can impede our interpretations on the lava properties and emplacement processes of lava flows on other planetary bodies, where no such ground truth data is available. We recommend that caution needs to be taken when studying the surface roughness and morphology of lava flows on other planetary bodies such as the Moon. By being conservative, we can begin to improve our understanding of volcanic surfaces on the Moon, which can be applied to future lander/rover missions with the objective to study lunar volcanism.

Acknowledgements

Field work was conducted with support from FINESSE (Field Investigations to Enable Solar System Science and Exploration), Jennifer L. Heldmann, PI, funded by the NASA Solar System Exploration Research Virtual Institute (SSERVI), and the National Park Service personnel at Craters of the Moon National Monument and Preserve (Permit #CRMO-2014-SCI-0004). We would also like to thank Ms. Rachel Maj, Mr. Kevin Fan, and Dr. Raymond Francis for their assistance in the field. Thanks also to Dr. Alex Selkhe for providing input on an earlier version of this manuscript. Special thanks to the Canadian Space Agency’s Flights and Fieldwork for the Advancement of Science and Technology program for funding this research, and to the Leverhulme Trust Committee (Account No. IND11814) for providing Gavin Tolometti with a scholarship to support his studies. Petrographic and geochemical analysis could not have been possible without the help from technical staff at Western University (Marc Beauchamp, Stephen Wood, and Dr. Charlie Wu).

References

Bondre, N.R., Duraiswami, R.A., Dole, G., 2004. A brief comparison of lava flows from the Deccan Volcanic Province and the Columbia-Oregon Plateau Flood Basalts : Implications for models of flood basalt emplacement. J. Earth Syst. Sci. 113, 809–817.

Campbell, B.A., 2012. High circular polarization ratios in radar scattering from geologic targets 117, 1–9. https://doi.org/10.1029/2012JE004061

Campbell, B.A., 2002. Radar Remote Sensing of Planetary Surfaces. Cambridge University Press.

Campbell, B.A., Campbell, D.B., Margot, J.-L., Ghent, R.R., Nolan, M., Chandler, J., Carter, L.M., Stacy, N.J., 2007. Focused 70-cm wavelength radar mapping of the Moon. IEEE Trans. Geosci. Remote Sens. 45, 4032–4042.

Campbell, B.A., Carter, L.M., Campbell, D.B., Nolan, M., Chandler, J., Ghent, R.R., Ray Hawke, B., Anderson, R.F., Wells, K., 2010. Earth-based 12.6-cm wavelength radar mapping of the Moon: New views of impact melt distribution and mare physical properties. Icarus 208, 565–573. https://doi.org/10.1016/j.icarus.2010.03.011

Campbell, B.A., Carter, L.M., Hawke, B.R., Campbell, D.B., Ghent, R.R., 2008. Volcanic and impact deposits of the Moon's Aristarchus Plateau: A new view from Earth-based radar images. Geology 36, 135–138. https://doi.org/10.1130/G24310A.1

Campbell, B.A., Hawke, B.R., Campbell, D.B., 2009. Surface morphology of domes in the Marius Hills and Mons Rümker regions of the Moon from Earth-based radar data. J. Geophys. Res. 114, 1–10. https://doi.org/10.1029/2008JE003253

Campbell, B.A., Hawke, B.R., Thompson, T.W., 1997. Long-wavelength Radar Studies of the Lunar Maria. Journal Geophys. Res. 102, 19,307-19,320.

Campbell, B. a, Shepard, M.K., 1996. Lava flow surface roughness and depolarized radar scattering. J. Geophys. Res. 101, 18,941-18,951.

Campbell, B., Hawke, B., Morgan, G., Carter, L., Campbell, D., Nolan, M., 2014. Improved discrimination of volcanic complexes, tectonic features, and regolith properties in Mare Serenitatis from Earth-based radar mapping. J. Geophys. Res. Planets 119, 313–330. https://doi.org/10.1016/S0733-8619(03)00096-3

Carter, L.M., Campbell, D.B., Campbell, B.A., 2011. Geologic studies of planetary surfaces using radar polarimetric imaging. Proc. IEEE 99, 770–782. https://doi.org/10.1109/JPROC.2010.2099090

Carter, L.M., Campbell, D.B., Campbell, B.A., 2006. Volcanic deposits in shield fields and highland regions on Venus : Surface properties from radar polarimetry. J. Geophys. Res. 111. https://doi.org/10.1029/2005JE002519

Carter, L.M., Campbell, D.B., Campbell, B.A., 2004. Impact crater related surficial deposits on Venus : Multipolarization radar observations with Arecibo. Journal Geophys. Res. 109. https://doi.org/10.1029/2003JE002227

Carter, L.M., Neish, C.D., Bussey, D.B.J., Spudis, P.D., Patterson, G.W., Cahill, J.T., Raney, R.K., 2012. Initial observations of lunar impact melts and ejecta flows with the Mini-RF radar. J. Geophys. Res. 117, 1–13. https://doi.org/10.1029/2011JE003911

Chin, G., Brylow, S., Foote, M., Garvin, J., Kasper, J., Keller, J., Litvak, M., Mitrofanov, I., Paige, D., Raney, K., Robinson, M., Sanin, A., Smith, D., Spence, H., Spudis, P., Stern, S.A., Zuber, M., 2007. Lunar Reconnaissance Orbiter Overview : The Instrument Suite and Mission. Space Sci. Rev. 129, 391–419. https://doi.org/10.1007/s11214-007-9153-y

Crisp, J., Baloga, S., 1994. Influence of crystallization and entrainment of cooler material on the emplacement of basaltic aa lava flows. J. Geophys. Res. 99, 11819–11831.

Duraiswami, R.A., Bondre, N.R., Managave, S., 2008. Morphology of rubbly pahoehoe (simple) fl ows from the Deccan Volcanic Province : Implications for style of emplacement. J. Volcanol. Geotherm. Res. 177, 824–838. https://doi.org/10.1016/j.jvolgeores.2008.01.048

Duraiswami, R.A., Gadpallu, P., Shaikh, T.N., Cardin, N., 2014. Pahoehoe-a'a transitions in the lava flow fields of the western Deccan Traps, India-implications for emplacement dynamics, flood basalt architecture and volcanic stratigraphy. J. Asian Earth Sci. 84, 146–166. https://doi.org/10.1016/j.jseaes.2013.08.025

Egghe, L., Rousseau, R., 1990. Introduction to Informetrics. Quantitative Methods in Library, Documentation and Information Science. Elsevier Science Publishers.

Evans, D.L., Farr, T.G., Ford, J.P., Thompson, T.W., Werner, C.L., 1986. Multipolarization Radar Images for Geologic Mapping and Vegetation Discrimination. IEEE Trans. Geosci. Remote Sens. GE-24, 246–257. https://doi.org/10.1109/TGRS.1986.289644

Faye, G., Miller, R., 1973. " Blue Dragon " Basalt from Graters of the Moon National Monument , Idaho : Origin of Color. Am. Mineral. 58, 1048–1051.

Fink, J. H., & Fletcher, R. C. (1978). Ropy pahoehoe: Surface folding of a viscous fluid. Journal of Volcanology and Geothermal Research, 4(1-2), 151-170.

Glaze, L.S., Baloga, S.M., 2007. Topographic variability on Mars: Implications for lava flow modeling. J. Geophys. Res. E Planets 112, 1–9. https://doi.org/10.1029/2006JE002879

Glenn, N.F., Streutker, D.R., Chadwick, D.J., Thackray, G.D., Dorsch, S.J., 2006. Analysis of LiDAR-derived topographic information for characterizing and differentiating landslide morphology and activity. Geomorphology 73, 131–148. https://doi.org/10.1016/j.geomorph.2005.07.006

Greeley, R., King, J.S., 1977. Volcanism of the eastern Snake River Plain, Idaho: A Comparative planetary geology-guidebook. Washington, D.C., NASA CR 154621.

Gregg, T.K.P., Fink, J.H., 1996. Quantification of extraterrestrial lava flow effusion rates through laboratory simulations. J. Geophys. Res. 101, 16891–16900. https://doi.org/10.1029/96JE01254

Gregg, T.K.P., Fink, J.H., 1995. Quantification of submarine lava-flow morphology through analog experiments. Geology 23, 73–76. https://doi.org/10.1130/0091-7613(1995)023<0073

Gregg, T. K., Fink, J. H., & Griffiths, R. W. 1998. Formation of multiple fold generations on lava flow surfaces: Influence of strain rate, cooling rate, and lava composition. Journal of Volcanology and Geothermal Research, 80(3-4), 281-292.

Griffiths, R.W., Fink, J.H., 1992. The morphology of lava flows in planetary environments: Predictions from analog experiments. J. Geophys. Res. 97, 19739. https://doi.org/10.1029/92JB01953

Guilbaud, M.-N., Self, S., Thordarson, T., Blake, S., 2005. Morphology, surface structures, and emplacement of lavas produced by Laki, A.D. 1783 – 1784. GSA Spec. Pap. 396, 81–102. https://doi.org/10.1130/2005.2396(07).

Hamilton, C.W., Glaze, L.S., James, M.R., Baloga, S.M., 2013. Topographic and stochastic influences on pāhoehoe lava lobe emplacement. Bull. Volcanol. 75, 1–16. https://doi.org/10.1007/s00445-013-0756-8

Harmon, J.K., Nolan, M.C., Husmann, D.I., Campbell, B. a., 2012. Arecibo radar imagery of Mars: The major volcanic provinces. Icarus 220, 990–1030. https://doi.org/10.1016/j.icarus.2012.06.030

Head, J. W., & Wilson, L. 2017. Generation, ascent and eruption of magma on the Moon: New insights into source depths, magma supply, intrusions and effusive/explosive eruptions (Part 2: Predicted emplacement processes and observations). Icarus, 283, 176-223.

Hughes, S.S., Kobs-Nawotniak, S.E., Borg, C., Mallonee, H.C., Purcell, S., Neish, C., Garry, W.B., Haberle, C.W., Lim, D.S.S., Heldmann, J.L., Team, the F., 2016. Diverse Eruptions at ~2,200 Years B.P. on the Great Rift, Idaho: Inferences for Magma Dynamics Along Volcanic Rift Zones. 47th Lunar and Planetary Science Conference, pp. 6–7.

Hughes, S.S., Smith, R.P., Hackett, W.R., Anderson, S.R., 1999. Mafic Volcanism and Environmental Geology of the Eastern Snake River Plain, Idaho. Guideb. to Geol. East. Idaho 143–168.

Hughes, S.S., Wetmore, P.H., Casper, J.L., 2002. Evolution of Quaternary Tholeiitic Basalt Eruptive Centers on the Eastern Snake River Plain , Idaho. Idaho Geol. Surv. Bull. 30, 1–23.

Keszthelyi, L., Mcewen, A.S., Thordarson, T., 2000. Terrestrial analogs and thermal models for Martian flood lavas. J. Geophys. Res. E Planets 105, 15,027-15,049. https://doi.org/10.1029/1999je001191

Keszthelyi, L., Thordarson, T., McEwen, A., Haack, H., Guilbaud, M.N., Self, S., Rossi, M.J., 2004. Icelandic analogs to Martian flood lavas. Geochemistry, Geophys. Geosystems 5, 1–32. https://doi.org/10.1029/2004GC000758

Khan, S., Essam, H., Jaime, F., 2007. Mapping exposed and buried lava flows using synthetic aperture and ground-penetrating radar in craters of the moon lava field. 2007 GSA Denver Annu. Meet. (28–31 Oct. 2007) 72, 123. https://doi.org/10.1190/1.2793298

Kolzenburg, S., Jaenicke, J., Münzer, U., & Dingwell, D. B., 2018. The effect of inflation on the morphology-derived rheological parameters of lava flows and its implications for interpreting remote sensing data-A case study on the 2014/2015 eruption at Holuhraun, Iceland. *Journal of Volcanology and Geothermal Research*, *357*, 200-212.

Kuntz, M.A., 1989. Geology of the Craters of the Moon Lava Field, Idaho, in: Ruebelmann, K.L., Smith, R.P., Downs, W.F., Christiansen, R.L., Hacket, W.R., Morgan, L.M., Leeman, W.P., Wood, S.H., Malde, H.E., Kuntz, M.A. (Eds.), Snake River Plain-Yellowstone Volcanic Province: Jackson, Wyoming to Boise, Idaho. pp. 51–61. https://doi.org/https://doi.org/10.1029/FT305p0051

Kuntz, M.A., Champion, D.E., Lefebvre, R.H., 1988. Geologic map of the Craters of the Moon, Kings Bowl, and Wapi Lava Fields, and the Great Rift Volcanic Rift Zone, south-central Idaho. U.S. Geol. Surv. Misc. Investig. Ser.

Kuntz, M.A., Champion, D.E., Spiker, E.C., Lefebvre, R.H., 2005. Contrasting magma types and steady-state, volume-predictable, basaltic volcanism along the Great Rift, Idaho (USA). Geol. Soc. Am. Bull. 97, 579–594. https://doi.org/10.1130/0016-7606(1986)97<579:CMTASV>2.0.CO;2

Kuntz, M.A., Covington, H.R., Schorr, L.J., 1992. An overview of basaltic volcanism of the eastern Snake River Plain, Idaho, in: Regional Geology of Eastern Idaho and Western Wyoming. Geological Society of America Memoir, 179, pp. 227–267.

Kuntz, M.A., Skipp, B., Champion, D.E., Gans, P.B., Van Sistine, P., Snyders, S.R., 2007. Geological map of Craters of the Moon 30' x 60' quadrangle, Idaho. US Geol. Surv. Sci. Investig. Map.

Kuntz, M. a, Champion, D.E., Spiker, E.C., Lefebvrelsd, R.H., Mcbroomes, L. a, 1982. The Great Rift and the Evolution of the Craters of the Moon Lava Field , Idaho. Cenezoic Geol. Idaho Idaho Bur. Mines Geol. Bull. 26, 423–437.

Kuntz, M.E.L.A., Survey, U.S.G., Champion, D.E., Survey, U.S.G., Park, M., Spiker, E.C., Survey, U.S.G., 1986. basaltic volcanism along the Great Rift , Idaho 579–594.

Lawrence, S.J., Stopar, J.D., Hawke, B.R., Greenhagen, B.T., Cahill, J.T.S., Bandfield, J.L., Jolliff, B.L., Denevi, B.W., Robinson, M.S., Glotch, T.D., Bussey, D.B.J., Spudis, P.D., Giguere, T.A., Garry, W.B., 2013. LRO observations of morphology and surface roughness of volcanic cones and lobate lava flows in the Marius Hills. J. Geophys. Res. E Planets 118, 615–634. https://doi.org/10.1002/jgre.20060

Leeman, W.P., 1982. Evolved and hybrid lavas from the Snake River Plain, in: Bonnichsen, B., Breckenridge, R.M. (Eds.), Cenozoic Geology of Idaho. Idaho Bureau of Mines and Geology, Bulletin 26, pp. 193–202.

Leeman, W.P., Vitaliano, C.J., Prinz, M., 1976. Evolved Lavas from the Snake River Plain. Contrib. to Mineral. Petrol. 56, 35–60.

Lejeune, A.M., Richet, P., 1995. Rheology of crystal-bearing silicate melts: An experimental study a high viscosities. Journal Geophys. Res. 100, 4215–4229.

MacDonald, G.A., 1953. Pahoehoe, Aa, and Blocky Lava. Am. J. Sci. 251, 169–191.

Mcewen, A.S., Eliason, E.M., Bergstrom, J.W., Bridges, N.T., Hansen, C.J., Delamere, W.A., Grant, J.A., Gulick, V.C., Herkenhoff, K.E., Keszthelyi, L., Kirk, R.L., Mellon, M.T., Squyres, S.W., Thomas, N., Weitz, C.M., 2007. Mars Reconnaissance Orbiter ' s High Resolution Imaging Science Experiment (HiRISE). Journal Geophys. Res. 112. https://doi.org/10.1029/2005JE002605

Morgan, G.A., Campbell, B.A., Campbell, D.B., Hawke, B.R., 2016. Investigating the stratigraphy of Mare Imbrium flow emplacement with Earth-based radar. J. Geophys. Res. 121, 1498–1513. https://doi.org/10.1002/2016JE005041.Received

Neish, C.D., Carter, L.M., 2014. Planetary Radar, in: Encyclopedia of the Solar System. pp. 1133–1159.

Neish, C.D., Hamilton, C.W., Hughes, S.S., Nawotniak, S.K., Garry, W.B., Skok, J.R., Elphic, R.C., Schaefer, E., Carter, L.M., Bandfield, J.L., Osinski, G.R., Lim, D., Heldmann, J.L., 2017. Terrestrial analogues for lunar impact melt flows. Icarus 281, 73–89. https://doi.org/10.1016/j.icarus.2016.08.008

Neish, C.D., Madden, J., Carter, L.M., Hawke, B.R., Giguere, T., Bray, V.J., Osinski, G.R., Cahill, J.T.S., 2014. Global distribution of lunar impact melt flows. Icarus 239, 105–117. https://doi.org/10.1016/j.icarus.2014.05.049

Patterson, G.W., Stickle, A.M., Turner, F.S., Jensen, J.R., Bussey, D.B.J., Spudis, P., Espiritu, R.C., Schulze, R.C., Yocky, D.A., Wahl, D.E., Zimmerman, M., Cahill, J.T.S., Nolan, M., Carter, L., Neish, C.D., Raney, R.K., Thomson, B.J., Kirk, R., Thompson, T.W., Tise, B.L., Erteza, I.A., Jakowatz, C. V., 2017. Bistatic radar observations of the Moon using Mini-RF on LRO and the Arecibo Observatory. Icarus 283, 2–19. https://doi.org/10.1016/j.icarus.2016.05.017

Peterson, D.W., Tilling, R.I., 1980. Transition of Basaltic Lava From Pahoehoe to AA, Kilauea Volcano, Hawaii: Field Observations and Key Factors. Journal Volcanol. Geotherm. Researc 7, 271–293.

Putirka, K.D., Kuntz, M. a., Unruh, D.M., Vaid, N., 2009. Magma evolution and ascent at the craters of the moon and neighboring volcanic fields, Southern Idaho, USA: Implications for the evolution of polygenetic and monogenetic volcanic fields. J. Petrol. 50, 1639–1665. https://doi.org/10.1093/petrology/egp045

Reid, M.R., 1995. Processes of mantle enrichment and magmatic differentiation in the eastern Snake River Plain: Th isotope evidence. Earth Planet. Sci. Lett. 131, 239–254.

Robert, B., Harris, A., Gurioli, L., Médard, E., Sehlke, A., Whittington, A., 2014. Textural and rheological evolution of basalt flowing down a lava channel. Bull. Volcanol. 76, 1–21. https://doi.org/10.1007/s00445-014-0824-8

Rosenburg, M.A., Aharonson, O., Head, J.W., Kreslavsky, M.A., Mazarico, E., Neumann, G.A., Smith, D.E., Torrence, M.H., Zuber, M.T., 2011. Global surface slopes and roughness of the Moon from the Lunar Orbiter Laser Altimeter 116, 1–11. https://doi.org/10.1029/2010JE003716

Rowland, S. K., & Walker, G. P. 1990. Pahoehoe and aa in Hawaii: volumetric flow rate controls the lava structure. Bulletin of Vol,canology, 52(8), 615-628.

Schaber, G. G., 1973. Lava flows in Mare Imbrium: Geologic evaluation from Apollo orbital photography. Geochimica et Cosmochimica Acta, 1, 73-92).

Sehlke, A., Whittington, A., Robert, B., Harris, A., Gurioli, L., Médard, E., Sehlke, A., 2014. Pahoehoe to áá transition of Hawaiian lavas: An experimental study. Bull. Volcanol. 76. https://doi.org/10.1007/s00445-014-0876-9

Shepard, M.K., Campbell, B.A., Bulmer, M.H., Farr, T.G., Gaddis, L.R., Plaut, J.J., 2001. The roughness of natural terrain: A planetary and remote sensing perspective. J. Geophys. Res. E Planets 106, 32777–32795. https://doi.org/10.1029/2000JE001429

Soldati, A., Sehlke, A., Chigna, G., Whittington, A., 2016. Field and experimental constraints on the rheology of arc basaltic lavas : the January 2014 Eruption of Pacaya (Guatemala). https://doi.org/10.1007/s00445-016-1031-6

Stout, M.Z., Nicholls, J., Kuntz, M. a, 1994. Petrological and mineralogical variations in 2500-2000 yr {B.P. Lava Flows, Crater of the Moon, Idaho}. J. Petrol. 35, 1681–1715.

Tilley, C.E., Thompson, R.N., 1970. MELTING AND CRYSTALL:ZAT10N RELATIONS OF THE

SNAKE RIVER BASALTS OF SOUTHERN IDAHO, USA. Earth Planet. Sci. Lett. 8, 79–92.

Ulaby, F.T., Begnal, T., East, J., Dobson, M.C., Garvin, J., Evans, D., 1988. Microwave dielectric spectrum of rocks. Report 23817-1-TU.

Whelley, P.L., Garry, W.B., Hamilton, C.W., Bleacher, J.E., 2017. LiDAR-derived surface roughness signatures of basaltic lava types at the Muliwai a Pele Lava Channel , Mauna Ulu , Hawai ‘ i. Bull. Volcanol. 79. https://doi.org/10.1007/s00445-017-1161-5

Whelley, P.L., Glaze, L.S., Calder, E.S., Harding, D.J., 2014. LiDAR-Derived Surface Roughness Texture Mapping : Application to Mount St . Helens Pumice Plain Deposit Analysis. IEEE Trans. Geosci. Remote Sens. 52, 426–438. https://doi.org/10.1109/TGRS.2013.2241443

Zanetti, M., Neish, C.D., Kukko, A., Choe, B.-H., Osinski, G.R., Tolometti, G.D., Fan, K., Maj, R., 2018. Surface Roughness and Radar Scattering Properties of Volcanic Terrain: Geologic Application of Kinematic Mobile LiDAR Scanning. InlLunar Planet. Sci. Conf. 49.

Zebker, H. A., & Lou, Y., 1990. Phase calibration of imaging radar polarimeter Stokes matrices. IEEE Transactions on Geoscience and Remote Sensing, 28(2), 246-252.